

AN EVALUATION OF THE FEASIBILITY OF THE TIME-LAPSE ELECTRICAL
RESISTIVITY TOMOGRAPHY METHOD IN QUANTIFYING SUBMARINE
GROUNDWATER DISCHARGE IN FINE SEDIMENT AND HIGHLY SALINE,
SHALLOW EMBAYMENTS

A Thesis

by

JOSEPH STEARNS

BS, Millsaps College, 2017

Submitted in Partial Fulfillment of the Requirements for the Degree of

MASTER OF SCIENCE

in

ENVIRONMENTAL SCIENCE

Texas A&M University-Corpus Christi
Corpus Christi, Texas

December 2019

© Joseph Ford Stearns

All Rights Reserved

December 2019

AN EVALUATION OF THE FEASIBILITY OF THE TIME-LAPSE ELECTRICAL
RESISTIVITY TOMOGRAPHY METHOD IN QUANTIFYING SUBMARINE
GROUNDWATER DISCHARGE IN FINE SEDIMENT AND HIGHLY SALINE
EMBAYMENTS

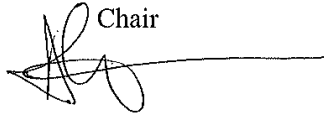
A Thesis

by

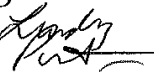
JOSEPH STEARNS

This thesis meets the standards for scope and quality of
Texas A&M University-Corpus Christi and is hereby approved.

Dorina Murgulet, PhD
Chair



Lindsay Prothro, PhD
Committee Member



Mohamed Ahmed, PhD
Committee Member



Deidre Williams
Committee Member



December 2019

Table of Contents

CONTENTS	PAGE
ABSTRACT.....	V
LIST OF FIGURES	VI
LIST OF TABLES	VIII
INTRODUCTION	1
1.1 Objectives	4
METHODS	5
2.1 Study Site.....	5
2.2 Experimental Methods	10
2.2.1 Time-Series Electrical Resistivity Tomography (ERT).....	10
2.2.2 Radioisotopes ^{222}Rn , ^{223}Ra , ^{224}Ra , and ^{226}Ra	19
2.2.3 Sediment Characterization	24
2.2.4 Hydrodynamic Model	25
RESULTS	27
3.1 Sediment Characterization.....	27
3.2 Hydrodynamic Model	27
3.3 Radioisotope SGD Calculations	32
3.3.1 Time Series ^{222}Rn -Derived SGD.....	32
3.3.2 Time Series ^{223}Ra , ^{224}Ra , and ^{226}Ra Derived SGD	36
3.4 Time-Series Electrical Resistivity Tomography (ERT) SGD Calculations.....	42
3.4.1 Model Accuracy Evaluation.....	42
3.4.2 Archie’s Law SGD Estimates	50
3.4.3 Waxman-Smits SGD Estimates	50
DISCUSSION	67
SUMMARY	72

ABSTRACT

There is uncertainty surrounding the application of the time-lapse electrical resistivity tomography (ERT) method in quantifying submarine groundwater discharge (SGD). The technique has been proven effective in areas with significant differences in salinity between surface water and discharging groundwater. However, there are inherent limitations associated with the method when studying embayments with fine bottom sediments, highly saline porewaters, and shallow surface waters. To evaluate this approach, a 68-hour time-lapse ERT study was conducted at University Beach (UB) in Corpus Christi, Texas, constrained by concomitant measurements of naturally occurring isotope tracers and groundwater characterizations along the ERT profile. Surface water continuous ^{222}Rn measurements were conducted to calculate SGD rates. Subsurface fluid conductivity measurements along the profile were constrained using inversion models via Archie's Law (AL) and the Waxman-Smiths equation (WSE). The average ERT-derived SGD rate for the study period was $26 \pm 1 \text{ cm} \cdot \text{d}^{-1}$. Average tracer-derived rates using the deep well endmember were 69 ± 26 , 49 ± 1 , 80 ± 2 , and $21 \pm 1 \text{ cm} \cdot \text{d}^{-1}$ corresponding to ^{222}Rn , ^{223}Ra , ^{224}Ra , and ^{226}Ra , respectively. Over the course of the study ^{222}Rn SGD estimates increased, while ERT and radium isotope estimates tended to decrease. There were no significant differences between the model accuracy of AL ($R^2=0.5$, $p<0.01$) and the WSE ($R^2=0.5$, $p<0.01$), thus there is no evidence that negatively charged clay particles in the subsurface matrix had any latent influence on the ERT measurements. Temperature, however, was found to be the predominant source of error in the ERT. The influence of temperature is often evident in the uppermost 1-2 m of images as temperature inflections drive the conductive recirculation of seawater. When temperature corrections were well constrained, the inversion models were significantly more successful at deriving modeled subsurface fluid conductivities closer to those observed, reducing error by up to 20%. Consequently, precise constraints on temperature are necessary to perform an effective experiment. ERT ultimately produced conservative SGD estimates relative to the radiogenic tracers. This is related to a lack of contrast between ambient and groundwater subsurface fluid conductivities. Thus, in the investigated environment, ERT may be used for qualitative and exploratory purposes, in the absence of other validating in-situ measurements.

LIST OF FIGURES

FIGURES	PAGE
Figure 1; Study Site (a) Gulf Coast Aquifer in blue, Oso Creek Watershed in red within the state of Texas in the United States of America. (b) Oso Creek Watershed in yellow and subwatersheds in green. (c) Location of study site with Corpus Christi Bay and Oso Bay for reference. (d) Aerial view of study site with sampling and equipment locations labeled. Satellite image taken from Google Earth.	7
Figure 2; Conceptual model of study site illustrating the subsurface stratigraphy and distribution of sample sites.	8
Figure 3; Graphic illustrating percent clay (a), silt (b), sand (c) and porosity (d) versus depth for well cutting sediment samples.....	29
Figure 4; Change in head over time illustrating the recovery of the (a) shallow ($K=1.98 \times 10^{-06} \text{ m}\cdot\text{s}^{-1}$) and (b) deep wells ($K=1.17 \times 10^{-06}$) during slug tests to determine hydraulic conductivity for Darcian SGD in Table 1.	30
Figure 5; Surface water height plotted with DTW in P6 measured by pressure transducer over time on secondary axis. There was found to be a six-hour lag correlation between surface water height and P6 DTW - R^2 (0.7984) and p-value (2×10^{-25}).	31
Figure 6; Time-series surface water ^{222}Rn activities plotted over time with 2-sigma uncertainty calculated in Capture, (a) vs. windspeed and (b) vs. tide. Gaps in data represent pump failure during data collection. Transparent orange portions indicate data collection was underway.	33
Figure 7; ^{222}Rn derived SGD rates for each endmember graphed for visual comparison.	36
Figure 8; (a) modeled pore conductivities graphed vs. ^{223}Ra ($R^2=0.0081$, p-value=0.9715, n=21) and (b) measured pore conductivities graphed vs. ^{223}Ra ($R^2=0.2376$, p-value=0.2984, n=21).	38
Figure 9; (a) modeled pore conductivities graphed vs. ^{224}Ra ($R^2=0.069$, p-value=0.766, n=21) and (b) measured pore conductivities graphed vs. ^{224}Ra ($R^2=0.7294$, p-value=0.0001, n=21).	39
Figure 10; Graphs of linear regressions performed in R for (a) Robust Waxman Model, (b) Robust Archie Model, (c) Smooth Waxman Model, (d) Smooth Archie Model, (e) Damped Waxman Model, and (f) Damped Archie Model.	44
Figure 11; Graphs of linear regressions performed in R for (a) Robust Archie Model (2) and (b) Robust Waxman Model (2) where outliers have been removed and temperature has been corrected.	45

Figure 12; Electrical resistivity tomograms for each timestep, processed in AGI EarthImager 2D using the robust inversion method (0.5 Ohm-m – 1.7 Ohm -m).....	46
Figure 13; Electrical resistivity percent difference images processed in EarthImager 2D (-20% - +20%). Calculated as $[(T_{n+1}-T_n)/T_n]*100$	47
Figure 14; Color relief electrical resistivity tomograms for each timestep, processed in surfer by kriging grid data exported from EarthImager2D (0.5 Ohm-m – 1.45 Ohm -m).	48
Figure 15; Color relief electrical difference images, processed in surfer by applying a kriging interpolation on grid data exported from EarthImager2D (-0.3 Ohm-m - +0.3 Ohm-m). Calculated as $T_{n+1}-T_n$. Time elapsed between timesteps labeled on figures.	49
Figure 16; Graphs of SGD rate over time for (a) Waxman-Smits equation and (b) Archie's Law.....	51
Figure 17; Piezometer 2 (a) measured conductivity plotted against modeled conductivity ($R^2=0.6547$, p-value=0.13394, n=6) and (b) measured temperature plotted against modeled conductivity ($R^2=0.0947$, p-value=0.8553, n=6).	52
Figure 18; measured conductivity plotted against modeled conductivity (a) Piezometer 1 ($R^2=0.1884$, p-value=0.0.7144, n=6); (b) Piezometer 3 ($R^2=0.2288$, p-value=0.6549, n=6); (c) Piezometer 4 ($R^2=0.0512$, p-value=0.0.9216, n=6); (d) Piezometer 6 ($R^2=0.0576$, p-value=0.9119).	53
Figure 19; measured temperature plotted against modeled conductivity (a) Piezometer 1 ($R^2=0.379$, p-value=0.4440, n=6); (b) Piezometer 3 ($R^2=0.784$, p-value=0.0449, n=6); (c) Piezometer 4 ($R^2=0.9335$, p-value=0.002); (d) Piezometer 6 ($R^2=0.4677$, p-value=0.3307).	54
Figure 20; Intercomparison of SGD rates with respect to each radiogenic isotope endmember. ^{223}Ra and ^{224}Ra in T1-T2 and T2-T3 in the deep well as well as ^{224}Ra for T1-T2 in the shallow well have been omitted from the graphs as they are more representative of a contrast in salinity rather than genuine SGD. Note that Darcian rates are <1 and difficult to decipher on this scale.	57

LIST OF TABLES

TABLES	PAGE
Table 1 – Darcian SGD rates calculated by applying the hydraulic conductivities obtained from slug tests above and measured hydraulic gradients.....	30
Table 2 – ^{222}Rn endmember activities in $\text{Bq}\cdot\text{m}^{-3}$. Samples were not collected at time steps T2, T3 and T5 from GWW, P1, P2 and P6. Error calculated as 2-sigma uncertainty via Capture.....	34
Table 3 – ^{222}Rn derived SGD rates for each endmember.	35
Table 4 – ^{223}Ra endmember activities ($\text{dpm}\cdot\text{m}^{-3}$) and associated 10% measurement error.	38
Table 5 – ^{224}Ra endmember activities ($\text{dpm}\cdot\text{m}^{-3}$) and associated 10% measurement error.	39
Table 6 – ^{226}Ra endmember activities ($\text{dpm}\cdot\text{m}^{-3}$) and associated 10% measurement error.	40
Table 7 – ^{223}Ra derived SGD rates for each endmember.....	41
Table 8 - ^{224}Ra derived SGD rates for each endmember.	42
Table 9 - ^{226}Ra derived SGD rates for each endmember.	42
Table 10 – Results of statistical analyses performed in R for each model including mean absolute error, Pearson correlation, linear regression, and nash-sutcliffe efficiency. As labeled, DA (Damped Archie), DW (Damped Waxman), RA (Robust Archie), RA (2) (Robust Archie sans outliers), RW (Robust Waxman), RW (2) (Robust Waxman sans outliers), SA (Smooth Archie), SW (Smooth Waxman).....	43
Table 11 – Archie’s Law ERT derived SGD rates.	50
Table 12 – Waxman-Smits ERT derived SGD rates.	50
Table 13 – Recorded water quality parameters, sample depths, collection times, and water levels (AMSL) for every sample throughout the survey.	55

1. Introduction

Submarine groundwater discharge (SGD) is a coastal hydrologic process defined as the flow of all types of water from the seabed to the coastal ocean, irrespective of the fluid composition or forces driving the interaction (Burnett and Dulaiova, 2003). The exchange of groundwater between terrestrial and marine environments is an important aspect of the hydrologic cycle which at times can be overlooked (Cardenas et al., 2010). Furthermore, SGD can play a significant role in the development of coastal ecosystems due to the potential for transport of anthropogenic contaminants and nutrients to coastal waters (Michael et al., 2003). Kohout and Kolipinski (1967) were among the first to investigate the biological significance of SGD. Their research identified a strong relationship between biological zonation and groundwater discharge into Biscayne Bay, Florida. For example, Marsh (1977) directly linked the presence of SGD with nutrient fluxes to coral reefs in Guam (Moore, 2010). In contrast, SGD can adversely affect coastal environments as well. Because nutrient loading in coastal groundwater can result in nutrient concentrations exponentially higher than surface waters, scientists have inferred that SGD may facilitate harmful algal blooms. Hu (2006) attributed long-lasting red tide conditions along the Florida coast in 2005 to Florida's active 2004 hurricane season which resulted in record amounts of precipitation and thus increased SGD. Given the wide-ranging effects of SGD, scientific research on this topic is necessary for a more comprehensive understanding of inherently dynamic coastal environments.

There are numerous methods which can be used to calculate and/or identify SGD. Scientists have employed geochemical tracer methods (radionuclides and dissolved CH₄),

physical methods (seepage meters), traditional Darcy flux calculations, and geophysical methods (electrical resistivity, seismic, and electromagnetics). Geochemical tracers and seepage meters currently provide the most effective means of obtaining SGD flux estimates, however, neither approach is completely precise or accurate. The geochemical tracer method unrealistically assumes uniform geologic controls and discharge over a broad area. It also does not account for hotspots or temporal variability (McCoy and Corbett, 2009). Seepage meters are an effective method of identifying localized points of SGD, but an inefficient means of quantifying it over an extended area. Lastly, Darcy's calculations tend to oversimplify the concept as it only accounts for freshwater inflow, ignoring the recirculated seawater component which has proven to be a substantial contributor to SGD in past investigations (Mulligan and Charette, 2006).

More recent studies have utilized the electrical resistivity method to study SGD by characterizing the subsurface distribution of salinity (Bighash and Murgulet, 2015; Breier et al., 2005; Manheim, 2004; Swarzenski, 2007). Investigation of SGD using electrical resistivity can prove challenging due to the complex geological conditions found along gulf coastlines and inherent limitations associated with the given methodology. One challenge related to this method can be subsurface composition. The above-mentioned studies, which have employed electrical resistivity tomography (ERT), have been performed in environments that receive significant recharge to aquifers and whose subsurface geology compliments the technique; i.e., volcanics, clean sands, etc. (Dimova et al., 2012; Manheim, 2004; Swarzenski, 2007). Fewer studies have been performed in arid or semi-arid climates with complex geology similar to the Texas Gulf Coast. Dimova (Dimova et al.) carried out an investigation on the volcanic island of Hawaii and found

tidal influence to be the primary driving force of SGD. As a result, discharge was locatable and predictable. Studying SGD in environments with inconsistent precipitation and heterogeneous soil with low hydraulic conductivities can prove to be more challenging for a variety of reasons. Driving forces can be less predictable (e.g., density driven, seasonal, changes in hydraulic gradient), hot spots can be more difficult to locate, salinity gradients may be indistinguishable, and the nature of the discharge so diffuse that resolution may be a limiting factor (Bighash and Murgulet, 2015).

As discussed in more detail in the *methods* section, several factors may contribute to the overall electrical structure of saturated sediments including changes in lithology, porosity and pore fluid salinity (Viso et al., 2010). Furthermore, the reliability of this method is dependent upon an adequate contrast in bulk resistivity as well as the spatial resolution of the imagery (Lewis F.D., 2006). In summary, there are various avenues for error in this type of investigation. This is problematic because the ultimate goal is to quantify SGD using these data. Erroneous and/or biased interpretations can lead to inaccuracies in SGD calculations by orders of magnitude. Lewis (2006) asserts that the use of synthetic models and resolution-matrix analysis is beneficial to identifying inversion artifacts and bias, thus establishing reasonable interpretations of the imagery.

While modelling and analysis have been proven effective, electrical resistivity alone is not always a sufficient means of delineating distribution of pore fluid composition. These types of investigations require the constraint of relevant parameters. Loke et al. (2013) assert that in their analysis of the effectiveness of electrical resistivity measurements, in-situ and/or laboratory testing of subsurface materials can be used to constrain the ER method. This sampling method can facilitate characterization of the

lithology and hydrogeology of the area of interest. In unconsolidated heterogeneous environments, similar to the Texas Gulf Coast, however, properly constraining entire profiles can be challenging. Consequently, a degree of spatial interpolation is necessary to analyze data, but any attempt at interpolating between points must be done with caution and the understanding that there is likely a degree of heterogeneity and anisotropy present in the subsurface.

Although performing these direct, *in situ* observations is ideal, other constraints such as seismic profiling are reliable ways to account for the subsurface geologic structure (Cross, 2010; Viso et al., 2010). Viso et al. (2010) coupled continuous resistivity profiles with seismic sub-bottom profiles to study SGD in Long Bay, South Carolina. This location is characterized by complex subsurface geology containing discontinuous strata which is disrupted by erosional truncations and relict paleochannels. It was observed in this study that paleochannel infill composed of coarse sediments can produce anomalous resistivities as a result of larger pore spaces. Ideally, seismic profiling can be used as a preliminary exploratory technique to provide stratigraphic control supplemented by direct observations.

1.1 Objectives

The primary objective of this study is to evaluate the application of electrical resistivity tomography concepts in calculating SGD in a coastal and well-mixed estuary with very fine bottom sediments, through constraint of several essential parameters associated with the methodology. More specifically, this study aimed to 1) identify errors and artifacts related to ERT data collection and processing; 2) determine how to correct for, or avoid, these errors and artifacts; and 3) optimize final SGD calculations associated with the method. Characterization of sediment at incremental depths will provide control

over the effects of changes in sediment type; namely porosity, percent clay, and cation-exchange capacity. Collection of detailed salinity data from locations spaced along the resistivity profile will aid in identifying changes in pore fluid composition. These sediment and salinity data can subsequently be used to produce forward models for the purpose of ground truthing. Application of multiple methods of processing and post-processing will help identify potential errors in current procedures. Lastly, constraining SGD measurements with four separate ^{222}Rn and $^{223/224/226}\text{Ra}$ mass balances would offer confidence in the results.

2. Methods

2.1 Study Site

University Beach is a restored beach that is located on a section of the south shore of Corpus Christi Bay in front of the Texas A&M University-Corpus Christi (TAMU-CC) campus, on Ward Island (Figure 1 & 2). The beach was restored through a collaborative effort between TAMU-CC, the Texas General Land Office and the City of Corpus Christi. According to the Conrad Blucher Institute for Surveying and Science (CBI) at TAMUCC, the beach was constructed in 2001 to restore a 366 m section of a more expansive beach that once extended along the entire shoreline fronting Ward Island. The beach had completely eroded approximately 60 years ago due to anthropogenic activity in the area that started in the 1930's with occupation of the area by the U.S. military. The 366 m long beach is stabilized on each end by terminal groins and protected from onshore forcing by three detached breakwaters (DBWs) that are oriented shore parallel in the nearshore. The application of the stabilizing structures both alongshore and offshore is otherwise known as a cellular design. This design provides stability to the system as it has not required re-

nourishment since it was put in place over 18 years ago using ~34,200 m³ of beach- quality quarry sand. This equates to approximately 1 m of sand in the vertical direction which has subsequently been naturally distributed seaward between the DBWs. While not evident in Figure 1, depositional features have formed perpendicular to the beach face directly behind each DBW. These features, when exposed, are referred to as tombolos, while the developmental stage of these features is referred to as a shoreline salient. A salient is a landform feature that protrudes from a relatively linear shoreline, typically in response to dampening of waves by an offshore structure such as a detached breakwater (DBW). The tombolos landward of each detached breakwater at UB formed gradually over time as the breakwaters sheltered the nearshore from erosion. There are seasonal variations, but the depositional features are generally submerged at high tide and exposed to some degree at low tide. While the surface water is shallow where the tombolos have formed, it has previously reached depths of approximately 1 m between the detached breakwaters (Williams, 2005).



Figure 1– Study Site (a) Gulf Coast Aquifer in blue, Oso Creek Watershed in red within the state of Texas in the United States of America. (b) Oso Creek Watershed in yellow and subwatersheds in green. (c) Location of study site with Corpus Christi Bay and Oso Bay for reference. (d) Aerial view of study site with sampling and equipment locations labeled. Satellite image taken from Google Earth.

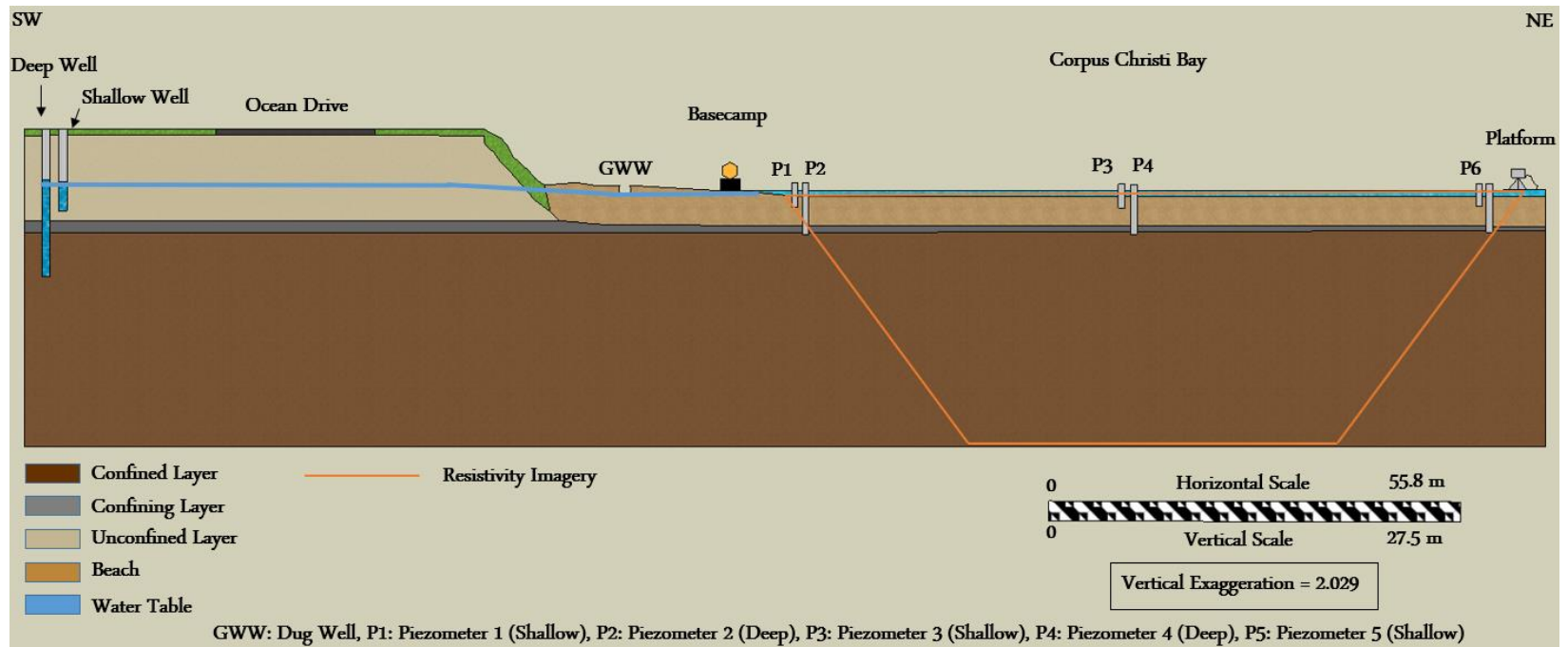


Figure 2 - Conceptual model of study site illustrating the subsurface stratigraphy and distribution of sample sites.

The formation of Corpus Christi Bay is attributed to the backfilling of an incised valley during a quaternary sea level transgression sequence in which sediment supply from local rivers did not keep pace with the associated sea level rise. The shallow bay is composed primarily of fine sand with a medium grain size diameter of 0.13 to 0.25 mm. Bay-center sediments are composed of fine silt and mud with a median grain size diameter ranging from 0.002 to 0.008 mm (R.A. Morton, 1979). In reference to Figure 1, Ward Island is a remnant of the Nueces River/Oso Creek deltaic complex. The top 14 ft of sediment in the subsurface is predominately clayey-silt and silty clay which is overlain by a thin surface layer of medium sized sand indicating a transgressive fluvial-estuarine sequence. Flores and Shindeler (Flores and Shindeler) indicated, using geochemical and mineralogical analyses on late quaternary sediment deposits within Corpus Christi Bay, Oso Bay, and the Upper Laguna Madre, that kaolinite and illite were present across all interpreted paleoenvironments, whereas smectite only occurred in the channel sediments and the undifferentiated kaolinite-chlorite occurred only in the channel and freshwater-upper bay sediments.

While geologic history and anthropogenic influence provide a broad understanding of the area, it must be corroborated with respect to the study site. There are two groundwater monitoring wells located on the lawn behind and across the street from UB. They were installed by the Center for Water Supply Studies (CWSS) approximately two years ago. The shallow well was drilled down to 6.1 m and screened up to 4.3 m. The deep well was drilled down to 12.2 m and screened up to 10.4m (Figure 2). Cuttings were collected from various depths when each well was drilled. In addition to the sediment data,

both wells are sampled by the TAMU-CC CWSS on a monthly basis. Samples were recorded in March 2018 and the salinity of the shallow well was determined to be 0.4 whereas the deep well was 49. For reference, the average salinity of sea water is approximately 35 (Millero, 2010).

The city of Corpus Christi, Tx is located in a semi-arid environment with November being a historically dry month. During the two weeks prior to the investigation, the study area received 5.41 cm of rainfall, with zero precipitation recorded in the 48 hours leading up to or during the sampling event (TWDB, 2018). Over the course of data collection, winds prevailed out of the southeast at an average of $3.1 \text{ m}\cdot\text{s}^{-1}$ with a maximum wind speed of $6.7 \text{ m}\cdot\text{s}^{-1}$ on November 17th (NOAA, 2018).

2.2 Experimental Methods

2.2.1 Time-Series Electrical Resistivity Tomography (ERT)

Electrical resistivity is a physical property which quantifies a material's resistance to the flow of electrical current. The ERT method is ideal for investigating near-surface processes and geologic structures because it relies on the premise that variations in fluid conductivity, as a result of changes in salinity, can be recorded as changes in the bulk resistivity along the profile (Zarroca et al., 2014). Furthermore, average resistivity values (Ohm-m) of natural materials range over a broad spectrum of numbers, providing certain materials with unique signatures (Palacky, 1988).

2.2.1.1 Survey Design & Data Collection

For the purpose of studying SGD, it was found beneficial to collect data over a full tidal cycle as tidal pumping could be the primary force driving the exchange of

groundwater and surface water at their respective sites (Dimova et al., 2012; Santos et al., 2009). This concept, however, is site dependent as not all environments experience tidal changes of the same magnitude. The domain of this study encompassed three full tidal cycles. ERT data was collected at each approximate peak and trough of the tidal cycles, resulting in six-time steps collected every 8-12 hours over a total of approximately 67 hours.

The disparity between salt and fresh water in the subsurface is the most important aspect of this technique for SGD measurements. During characterization of the fresh-water salt-water interface, for instance, variations in the composition of subsurface fluids is directly measured using the electrical current, which illustrates the porewater salinity/resistivity distribution. With respect to underwater ERT, measured resistivity anomalies, however, can be attributed not only to changes in lithology but ambient temperature and surface water depth and salinity (Vasantrao et al., 2017). Accordingly, in order to perform an effective experiment, it is important to constrain rock/soil type and changes in the fluid composition with time.

Two techniques have been used to study SGD using electrical resistivity: stationary time-series (or time-lapse) ERT (Swarzenski et al., 2006) and continuous (or mobile) resistivity profiling (CRP) (Murgulet et al., 2016). This study focused on the stationary time-series method.

Electrical resistivity data was collected using an Advanced Geosciences Inc. Supersting R8 supplemented with a 112 m, 56 graphite-electrode cable. The cable was deployed perpendicular from the beach face, weighted down and submerged to the

sediment-water interface. Data was collected using a dipole-dipole configuration, a method widely used by researchers in the study of SGD (Dimova et al., 2012); (Loke and Lane Jr, 2004); (Loke et al., 2013). Advantages of the dipole-dipole array over others are: (1) increased sensitivity to horizontal changes, which make it useful for lateral groundwater movement analyses; (2) maximum current efficiency, and (3) reduced error related to inductive coupling (Cross, 2010; Dimova et al., 2012; Harrison, 2006; Henderson et al., 2009; Orlando, 2013). In this configuration, as current is applied to the system, two fixed-current electrodes are assigned and voltage potentials are then measured across all remaining electrodes (Cross, 2010).

2.2.1.2 Processing

Consecutive resistivity images over an extended period of time (at different time-steps) along the same profile facilitate the production of time-step difference images in post-processing. Processing and interpretation of these images is based on the assumption that changes in bulk resistivity observed between each time step could be related to variations in the chemistry of the pore fluid, given the subsurface lithology is constant (Ogilvy, 2009).

An effective and efficient workflow for processing ERT data begins with a fundamental understanding of geophysical inverse problems, as previously detailed by Lines & Treitel (1984). During the inversion process of geophysical data, the software attempts to statistically correlate the response of a synthetic, a priori, earth model to measured values. Through an iterative process, the software manipulates model parameter estimates until the model response reaches a best fit to observed data. As geophysical data

are finite and ambiguous by nature, the solution to a geophysical inversion is inherently nonunique. While nonuniqueness is a very real obstacle to any geophysical survey, it can be leveraged to a certain degree during processing and interpretation.

There are three types of inversion available for processing in EarthImager 2D: damped least squares (DLS), smooth model, and robust. DLS is a nonlinear least-squares inversion method whereby the model and its parameters are iteratively updated. In between each iteration, the sum of the squares of the error between the model and observed values is calculated. This process continues until this error breaches a preset threshold (Lines & Treitel, 1984). The smooth model method attempts to solve a geophysical inversion problem explicitly for a predetermined model, relying on the accuracy of prior knowledge about the subsurface. It aims to objectively define the amount of fit the model can sacrifice for complexity. Lastly, a robust inversion differs from the previous two in that it utilizes an L1-norm to fit the model to the data. This statistical approach calculates the absolute differences of data misfit as opposed to squared differences, thereby reducing the influence of severe outliers on data quality (Day-Lewis et al, 2008). As each method has various strengths and weaknesses, Day-Lewis et al (2008) recommend employing each one during data processing. The researchers contend that this can help identify potential artifacts. If a feature which does not agree with constraints is present in one tomogram, but not the others, then it is more likely to be an artifact and must be subject to closer inspection during interpretation.

First, AGI Earthimager 2D combined the raw 800 millisecond (ms) diagonal readings to produce a measured apparent resistivity pseudosection. The data were then

trimmed by removing noisy electrodes and background noise along the profile. An underwater terrain (UWT) file was constructed with respect to changes in water column depth (i.e., tidal height and temperature) during each time step. This file contains the average water resistivity along the profile as well as overlying water thickness at all 56 electrodes. It is then attached to the raw geophysical data prior to the inversion in order to constrain the surface water layer. Each time step was inverted via the damped least squares (DLS) method, smooth model method, and robust method. When inverting the data, the software creates a rectangular grid where each square of the grid is assigned its own resistivity value representing a weighted average of that area. This is referred to as the “true” resistivity model (Loke and Lane Jr, 2004). Following the first inversion, data which misfit above the 10% threshold was removed and the inversion was performed a second time or until a quality model had been produced.

Subsequently, each time stamped section was processed through a difference inversion to calculate a percent change in resistivity spatially and temporally across the imagery. During this process the mesh values of the base image are subtracted from the subsequent image, then divided by the base image. The EarthImager2DManual (2009) asserts that this process can cancel any artifacts present in both images. These data, however, were not used for the final SGD calculations. They were used only for reference in interpretation. Instead, an XYZ file for each time step was loaded into the Surfer software where an algebraic difference tool was used to produce the final difference images for quantitative purposes. As previously mentioned, under the assumption that the lithology of the subsurface itself is not changing, it can be assumed that any difference in resistivity

over time should be attributed to changes in pore fluid chemistry. These difference images were, thus, used to calculate a net flux of groundwater discharge based on the RMS error of the base and monitor images. If the net change in the difference image exceeded the RMS error of both the base and monitor images, then the change could be defined as meaningful and used in calculations. A 2D polygon of each plume was created to calculate surface area (m^2), in the vertical direction, which was applied in equations 1-7. The plume area was multiplied by a 1 m, areal extent, to produce a flux ($m^3 \cdot d^{-1}$), as homogeneity is assumed 1 m into the section (Collette, 2006).

2.2.1.3 Archie's Law

Traditionally, Archie's Law has been used to calculate SGD by the electrical resistivity method. Collette (2006) details the components of Archie's Law for method correction in estimates of gas hydrate saturation in shaly-sands (Collette, 2006). For formation factor (F), the equation takes into account the tortuosity (a), porosity (Φ), and cementation (m) of the subsurface matrix. Tortuosity is a ratio which characterizes diffusive flow in porous media, porosity quantifies the amount of void space in between sediments, and the cementation exponent is a subsequent function of porosity (Onovughe, 2016). The formation factor is then used in conjunction with the resistivity of the saturated formation (Oberdorfer) in order to determine the resistivity of the pore fluid. Once the pore fluid has been characterized, salinity can be obtained and, thus, a final calculation for the volume of groundwater discharge.

- $F = (a)(\varphi^{-m})$ (1)
 - F: formation factor
 - a: tortuosity factor (lithology coefficient) = $0.0012 * (\% \text{ clay}) + 1$

- Φ : porosity
- m: cementation exponent ($>$ permeability = $<$ m)
- $R_p = R_f/F$ (2)
 - R_p : resistivity of pore fluid
 - R_f : resistivity of saturated formation
- $S = 7.042 \times R_p^{-1.0233}$ (3)
 - S: salinity
- $Q_{gwd} = V_{sal}[(S_1-S_2)/S_2] / \Delta t$ (4)
 - Q_{gwd} : volume of groundwater discharge
 - V_{sal} : volume derived from area of polygon feature in ArcMap
 - S: 1 is initial 2 is final
 - Δt : time elapsed

2.2.1.4 Waxman-Smits Equation

Onovughe (2016) found that when shale is present in sand, the ERT method tends to result in an inaccurate estimation of fluid content. Thus, the Waxman-Smits Model, which is a modified extension of Archie's Law, can be applied to shaly-sands because it takes into account the additional measured bulk electrical conductivity that is created by clays. The model quantifies the specific cation conductance (B) as well as the cation exchange capacity (CEC) (QV) as shown in the following equations (Onovughe, 2016):

- $R_f = \phi^{-m} R_p / (1 + R_p * B * Q_v)$ (5)
 - R_f : resistivity of formation
 - ϕ^{-m} : tortuosity factor = $0.0012 * (\% \text{ clay}) + 1$
 - R_p : resistivity of pore fluid
 - B: specific cation conductance (meq/mL) -> is salinity and temperature dependent
 - Q_v : cation exchange capacity (meq/mL).
- $S = 7.042 \times R_p^{-1.0233}$ (6)
 - S: salinity
- $Q_{gwd} = V_{sal}[(S_1-S_2)/S_2] / \Delta t$ (7)
 - Q_{gwd} : volume of groundwater discharge
 - V_{sal} : volume derived from area of polygon feature in ArcMap
 - S: 1 is initial 2 is final
 - Δt : time elapsed

Soils and sediments may possess electrostatic charge due to atomic substitution in the lattices of constituent minerals resulting in a net negative charge as well as hydrolysis reactions on the broken edges of the lattices and the surfaces of oxides, hydroxides, hydrous oxides, and organic matter (Gregorich, 2006; Hunt, 1981). The latter mechanism's role in this process results from the decrease in adsorption with decreasing pH (where H^+ ions compete with cations on the surface) and an increase in CEC coinciding with an increase in relative surface area (or decrease in particle size) (Eby, 2004). When this net negative charge is formed, exchangeable counterions (an ion in solution that associates itself with an ion of opposite charge on the surface of a member of a solute) are attracted and form the exchange complex. In summary, CEC is a measure of the number of ions that can be adsorbed, in an exchangeable fashion, on negative charge sites within the matrix (Bache, 1975; Carroll, 1959; Gregorich, 2006). There are multiple methods of determining CEC, namely characterization by color and texture of sediments (Eby, 2004).

2.2.1.5 Forward Modeling and Groundtruthing

Constraints were applied to forward models and used to evaluate the accuracy of ERT in a hypersaline and shallow marine environment with fine-grained bottom sediment, using the sediment characteristics (i.e., grain size, porosity, permeability, and CEC), detailed salinity data, surface water thickness, and temperature data. Firstly, theoretical salinity point values were reverse calculated from modeled resistivity values at piezometer locations on the resistivity profiles (Equation 6). Subsequently, salinity values were converted to specific conductivity (Equation 8) and corrected for temperature (Equation 9) (Manheim et al., 2004; Hayley et al., 2007). Notably, Hayley et al. (2007) found that

accounting for changes in temperature is essential in investigations that attempt to quantify moisture content or compare long-term time-lapse imagery, both of which are the premise of this survey. These data were then compared with the in-situ conductivity measurements at each piezometer in order to evaluate the accuracy of the ERT method in this environment given that artifact occurrence was a primary concern, specifically with respect to the high resolution near-surface portion of the imagery.

- $X_{25,S} = (S/35) * (53087) + S(S-35) * [J_1 + (J_2 * S^{1/2}) + (J_3 * S) + J_4 * S^{3/2}]$ (8)
 - X: Conductivity ($\mu S \cdot cm^{-1}$)
 - S: Salinity (ppt)
 - J₁: -16.072
 - J₂: 4.1495
 - J₃: -0.5345
 - J₄: 0.0261
- $EC_t = EC_{25} [1 + a(t-25)]$ (9)
 - a: temperature compensation factor (0.0185)
 - EC₂₅: electrical conductivity at 25 °C ($\mu S \cdot cm^{-1}$)
 - t: observed temperature (°C)

Models were evaluated for accuracy and precision using a variety of statistical analyses. These include linear regression, Pearson's product moment correlation, Nash-Sutcliffe Efficiency (Loggers), and mean absolute error (MAE) (Moriassi et al., 2007).

In addition, the in-situ data collected were used to produce full 2D forward models, which are representative of the study site for each time step. Point values were calculated around each piezometer, where physical measurements were obtained, and a linear gradient was applied between each piezometer to interpolate between sampling locations. In the deeper portions of the models where it was not possible to obtain in-situ constraints, sediment characterization and salinity data were correlated across the length of the profile from the deep and shallow wells located approximately 150 m to the south of the profile.

Grab water samples for ^{222}Rn were collected, with no head space, in 250 mL glass bottles for interstitial water in accordance with methodology provided by Durrige Co., Inc. (Murgulet et al., 2016). Surface water ^{222}Rn , however, was monitored continuously via a Durrige Rad7 Electronic Radon Detector and RadAqua accessory stationed behind the middle breaker within the cell, approximately 50 m from the resistivity cable and piezometers.

2.2.2 Radioisotopes ^{222}Rn , ^{223}Ra , ^{224}Ra , and ^{226}Ra

Radium (^{223}Ra , ^{224}Ra , ^{226}Ra) and radon (^{222}Rn) were used as geochemical tracers with the intent of deriving the fresh submarine groundwater discharge (FSGD) and recirculated submarine groundwater discharge (RSGD) components of SGD within the study area. Radium and radon are both products of the uranium-thorium decay series and are, thus, pervasive in local sediments. Because of this, coastal groundwater commonly contains higher activities when compared to ocean water, making these radioisotopes effective geochemical tracers of SGD (Baudron et al., 2015). More specifically, fresh groundwater is generally radium poor and must either attain longer residence times or mix with more saline sources to facilitate the desorption and enrichment of Ra isotopes. Consequently, it remains unlikely that any fresh groundwater advected across the sediment-water interface is detected via the radium method, and thus resultant SGD rates are more representative of saline circulation through coastal sediments. In turn, ^{222}Rn is a noble gas, so variations in salinity have no influence on activities. Therefore, SGD measurements obtained using ^{222}Rn are representative of both the fresh and recirculated components (Abraham et al., 2003; Baudron et al., 2015; Knee et al., 2016). Mulligan and

Charette (2006) applied both techniques and found the difference between the total and fresh estimates in good agreement with the radium-based method. In addition to hydrogeologic estimates, they concluded that the radon and radium techniques are in fact complimentary in estimating the different components of SGD.

2.2.2.1 Water Sample Collection

Water samples were collected from multiple sources during the experiment: (1) sediment interstitial fluid from five screened PVC piezometers installed at 1 m and 3 m depth extending perpendicular from the shoreline along the ERT profile; (2) surface water at the most nearshore nest of piezometers; (3) shallow groundwater from a dug well (approximately 1 m deep) at the beach face, (4) samples from the two terrestrial wells developed in each sub unit (Figure 2). Surface water samples were collected from approximately 0.2 m above the sediment-water interface. Water samples from piezometers and wells were collected after being purged three volumes worth of the piezometer tubing or well casing, respectively, or until field parameters stabilize on the YSI Pro Plus. Porewater and groundwater samples were obtained using silicon tubing connected to a peristaltic pump (Charette, 2006).

Water quality parameters and water levels/depth to water were collected for every sample using an YSI Pro Plus for temperature, pressure, dissolved oxygen, specific conductivity, salinity, pH, and ORP. After the water level and YSI data were accurately recorded, samples were collected for radiogenic isotopes. For the shallow well, deep well, surface water, piezometer three (P3), and piezometer four (P4), radioisotopes were collected at all six time-steps. For the dug well on the beach face (GWW), piezometer one

(P1), piezometer two (P2), and piezometer six (P6), radioisotopes were only collected at time-steps one (T1), four (T4), and six (T6). The aforementioned items were collected approximately every 8-12 hours starting at high and low tides.

2.2.2.2 ²²²Rn Derived SGD

A DurrIDGE RAD-7 radon-in-air detector was used to measure ²²²Rn activities for each type of radon grab sample collected as well as continuous surface water measurements for the duration of the 24-hour sampling event (DurrIDGE Co., Inc. Rad-7, RAD AQUA). As previously mentioned, continuous surface water measurements were collected using the permanent monitoring platform installed behind the middle breaker. Each data point recorded during the continuous survey is representative of an integrated signal, as the RAD7 cycle was set to 30 minutes.

Ultimately, ²²²Rn SGD rates were calculated based on a box model of the ²²²Rn inventory over time, accounting for mixing (+/-), atmospheric evasion (+), ²²⁶Ra supported ²²²Rn (-), and sediment supported ²²²Rn (-) (Equation 8). After each component has been accounted for, the remaining ²²²Rn inventory is assumed to be explained by the discharge of groundwater carrying excess ²²²Rn. The ratio of advective ²²²Rn flux to the ²²²Rn groundwater or porewater endmember activity determines the final seepage flux (Equation 10). While this serves as a brief summary of the method, a more thorough description has been detailed by several authors including (Moore and Arnold, 1996), (Burnett and Dulaiova, 2003), and (Smith, 2012).

- $F_{total} = (((C_{Rn} - C_{Ra}) * h) / \Delta t) - F_{sed} + F_{atm} \pm F_{mix}$ (9)
 - F_{total} : radon flux
 - C_{Rn} : ²²²Rn activity (Bq·m⁻³)

- C_{Ra} : ^{222}Rn supported by the decay of ^{226}Ra ($\text{Bq}\cdot\text{m}^{-3}$)
- h : water Depth (m)
- Δt : time elapsed over duration of measurements (days)
- F_{sed} : diffusive flux from sediment
- F_{atm} : flux lost across the air-sea boundary
- F_{mix} : ^{222}Rn flux through horizontal inflows or outflows
- $\omega = F_{total}/^{222}\text{Rn}_{gw}$ (10)
 - ω : groundwater seepage rate ($\text{cm}\cdot\text{d}^{-1}$)
 - $^{222}\text{Rn}_{gw}$: groundwater endmember activity

2.2.2.3 ^{223}Ra , ^{224}Ra , ^{226}Ra Derived SGD

Radium isotope data (^{223}Ra , ^{224}Ra , and ^{226}Ra) were obtained from surface, pore and groundwater samples according to methods established by Moore and Reid (1973). Large volume samples of approximately 40 L were collected for surface water, 20 L for wells, and 4 L for the pore water samples. The water samples were pumped slowly ($1\text{ L}\cdot\text{min}^{-1}$) through a cartridge with Mn-impregnated acrylic fibers, which are used to extract radium from the water (Moore and Reid, 1973). The fibers were then rinsed with radium-free water to remove all particles, dried to a wet weight between 20 and 30 g, and placed in a clean air tight cartridge to be run on a radium delayed coincidence counter (RADECC) for measurements of ^{223}Ra and ^{224}Ra (Moore and Arnold, 1996). Given that the half-lives of ^{223}Ra and ^{224}Ra are 11.4 days and 3.66 days, respectively, all samples were processed and run on the RADECC within three and a half days. Next, the same samples were flushed with Nitrogen (N) gas, sealed airtight, and stored for 21 days to allow for secular equilibrium which facilitated the ingrowth of ^{222}Rn from ^{226}Ra . Lastly, each sample cartridge was connected via a closed loop system to a DurrIDGE RAD7 which measured the ^{222}Rn as a proxy for ^{226}Ra (Kim, 2001).

Radium derived SGD rates were calculated based on a radium time series model developed by Peterson and Burnett et al (2008). The model assumes the only inputs of radium into the system to be desorption from suspended sediments, desorption and diffusion from bottom sediments, and advection of groundwater at the surface. Riverine inputs are neglected as there are no significant rivers discharging in the area. The offshore “endmember” component is excluded as well. Instead, the lowest activity measured during the course of the survey is used to represent the entire system’s background radium activity. As it is likely that at least a portion of this measurement is a product of SGD, this is a generous estimate of radium produced by sources other than SGD and thus will yield conservative SGD rates. The only significant sink for radium is mixing.

In performing the calculations, each measured radium activity ($R_{a_{total}}$) is adjusted by subtracting out the background activity ($R_{a_{bkgd}}$). As this value is taken from the lowest measured radium activity during the survey, it is also assumed to account for any contribution from bottom or suspended sediments. The difference is then multiplied by the measured water depth (d) to convert the value from an excess activity to an excess inventory. The product is then divided by the estimated residence time (τ) to obtain a flux of radium. Lastly, the quotient is divided by an established groundwater endmember radium activity ($R_{a_{gw}}$) to produce a water flux.

- $SGD(m \cdot d^{-1}) = \{[R_{a_{total}} - R_{a_{bkgd}}] \times d\} / [\tau \times R_{a_{gw}}]$ (11)
 - $R_{a_{total}}$: measured radium activity ($dpm \cdot m^{-3}$)
 - $R_{a_{bkgd}}$: lowest measured activity ($dpm \cdot m^{-3}$)
 - D : water depth (m)
 - τ : residence time (days)
 - $R_{a_{gw}}$: groundwater endmember radium activity

2.2.3 Sediment Characterization

Borehole cuttings were collected in intervals (4.88, 5.34, 5.79, 5.95, 7.31, 9.15, 10.37, 12.19 m bgs) during installation of the monitoring wells. Bulk density porosity tests and a grain size analysis were performed on each interval of cuttings in order to determine the percent distribution of sediment in the matrix. Data on sediment type in Corpus Christi Bay are available from (Flores and Shindeler, 1986). However, it is more beneficial to perform a site-specific characterization due to the heterogeneity of the subsurface in the area.

For porosity measurements, samples ~5 cm in height of saturated sediment from each interval were weighted and dried in an air-forced lab oven at 105° C until completely dry (indicated by no further change in mass). Porosity was determined using the relationship between bulk and particle density (Avnimelech et al., 2001).

$$\bullet \quad \phi = 1 - \frac{\rho_b}{\rho_g} \quad (12)$$

- ϕ : porosity
- ρ_b : bulk density (g·cm⁻³)
- ρ_g : particle density (g·cm⁻³)

The grain size distribution analyses were performed using the laser diffraction method (Beckman Coulter with a Limit of Detection (LOD): 0.375μm – 2000μm) on 1-2 cm³ of sediment sample from each section of the core. After partitioning of sediment samples in approximately 10 or more intervals (for a 1 m sediment core), organic matter was removed from the matrix using hydrogen peroxide in a progressive manner (up to 40% by volume), in order to control the rate of reaction (Welschmeyer, 1994), until digestion in the sample ceased. Subsequently, the samples were washed with deionized water, agitated,

and centrifuged two times for approximately 20 minutes each before performing the instrumental analyses. Prior to the instrumental analyses, the centrifuge tubes were checked to confirm that the supernatant was transparent, ensuring that all of the fine particles in the sample had settled out of solution.

2.2.4 Hydrodynamic Model

Slug tests were conducted in the two monitoring wells located behind the beach face. Methodology was derived from several sources: (ASFT&M, 1999; BENTALL, 1936; Leslie W. Lenfest, 2012; USGS, 2010). Testing began by recording an initial water level measurement of the well. Next, water was pumped from the well into a flow through cell containing an YSI multi-parameter probe. Water was pumped from the well until readings stabilized. All parameters were recorded, but salinity was specifically noted as it is necessary for setting logging parameters. The water level in the well was allowed to recover back to the initial measurement.

A LevelTroll 700 Sonde was lowered into the well until fully immersed at the top of the water column. The water was again allowed to stabilize, and pressure/temperature logging began using the Win-Situ 5 program. A slug (i.e. a PVC pipe that has been filled with sand and capped) was rapidly lowered into the well until it was fully immersed beneath the sonde, but not blocking the screen. The sonde recorded pressure/temperature data every 5 seconds, until the recharge rate had slowed to less than 0.01 meters every 10 minutes, upon which the slug was quickly and carefully removed from the well to allow for a slug out test.

Upon completion of the slug tests, data were downloaded off the sonde and processed in Microsoft Excel according to the Hvorslev method (Fetter, 2001) (Equation 13). The first step in processing these data was identifying the exact moment at which the slug was immersed, capturing the initial peak in head (h_0). Next, a column was constructed for the recovery ratio (h/h_0) which helps illustrate the rate of recovery in the well. Finally, t_{37} is picked from the data, representing the time it took for the water level to decrease to 37% of the initial change in head to ultimately calculate an accurate hydraulic conductivity (K).

- $\phi = K = (r^2 \ln(L_e/R)) / (2 * L_e * t_{37})$ (13)
 - r: radius of well casing
 - R: radius of well screen
 - L_e : length of well screen
 - t_{37} : time for water level to reach 37% of initial change in head

In addition to slug tests, the transducers were installed in the shallow well, deep well, and piezometer number six (P6) during the survey in order to compile a complete record and observe any potential anomalies which may occur. This was, in part, due to unusual salinity data in the wells which had been collected over the course of multiple sampling events in the previous 8-10 months where the water would transition from fresh to hypersaline, or vice versa, between surveys. The transducers were installed to continuously monitor depth to water in the shallow well, deep well, and P6 approximately one hour before the very first sample of the survey was collected. They were left in place for another two days following the collection of the final sample.

3. Results

3.1 Sediment Characterization

The grain size analysis agreed with the initial hypothesis of the subsurface structure whereby a clay confining layer approximately 6.1 m deep separates two silty sand, water bearing formations. The bulk density porosity (n) experiment supported this idea as these data showed a relative peak porosity of 0.52 at 6.1 m depth, suggestive of fine to ultra-fine materials (Figure 3).

Slug tests performed in both the deep and shallow units yielded hydraulic conductivities of 1.17×10^{-06} and $1.98 \times 10^{-06} \text{ m}\cdot\text{s}^{-1}$, respectively, magnitudes associated with silty sand units (Fetter, 2001) (Figure 2, 3, 4). While both the shallow and deep well have been described as being located in their own unique beds, the similarity in hydraulic conductivities is not unusual as each bed is likely to share lithology at this scale.

3.2 Hydrodynamic Model

There were no significant changes in water levels in the shallow and deep wells during data collection. Water levels in the shallow well ranged from 1.3 m to 1.4 m above mean sea level (AMSL), whereas the deep well ranged from 1.6 m to 1.7 m AMSL. There may be larger scale trends related to the hydraulic heads in the wells, but none were observable over this relatively short period of time. As a result, Darcian discharge values remain consistent in both wells, ranging from $0.40 - 0.48 \text{ cm}\cdot\text{d}^{-1}$ (Table 1).

A significant positive lagged correlation occurs between the water level (DTW) in P6 and the height of the surface water at six hours ($R^2=0.80$, $p\text{-value}=2 \times 10^{-25}$) (Figure 5). The six-hour delay is related to the ability of the subsurface medium to transmit water and

respond to the change in hydraulic head (i.e., high tide leads to lower hydraulic gradients towards the estuary). This response indicates that a hydrologic connection exists between the shallow bay and the subsurface in the study area, feedback observed in response to a maximum tidal change of 0.2 m.

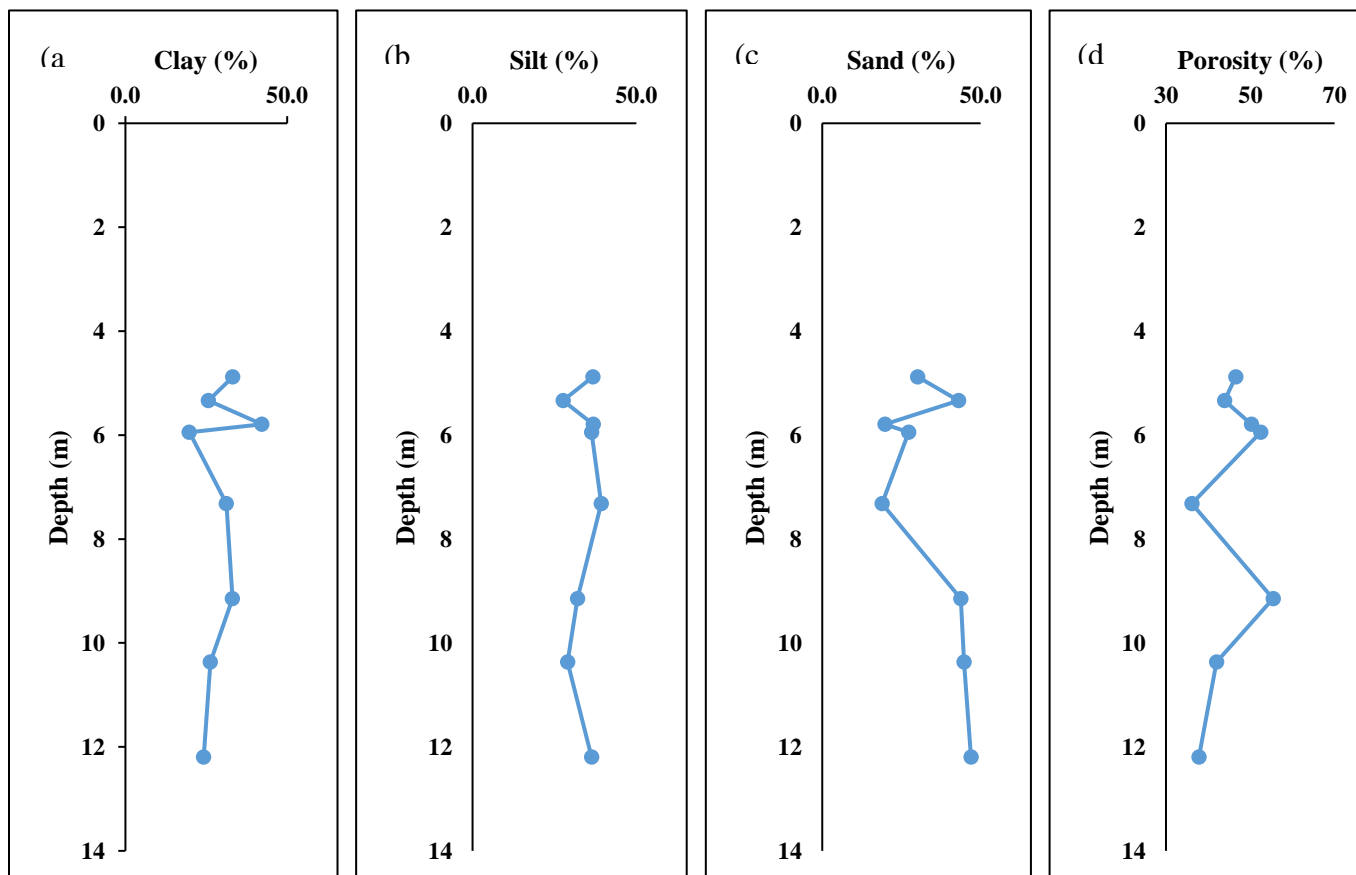


Figure 3 – Graphic illustrating percent clay (a), silt (b), sand (c) and porosity (d) versus depth for well cutting sediment samples.

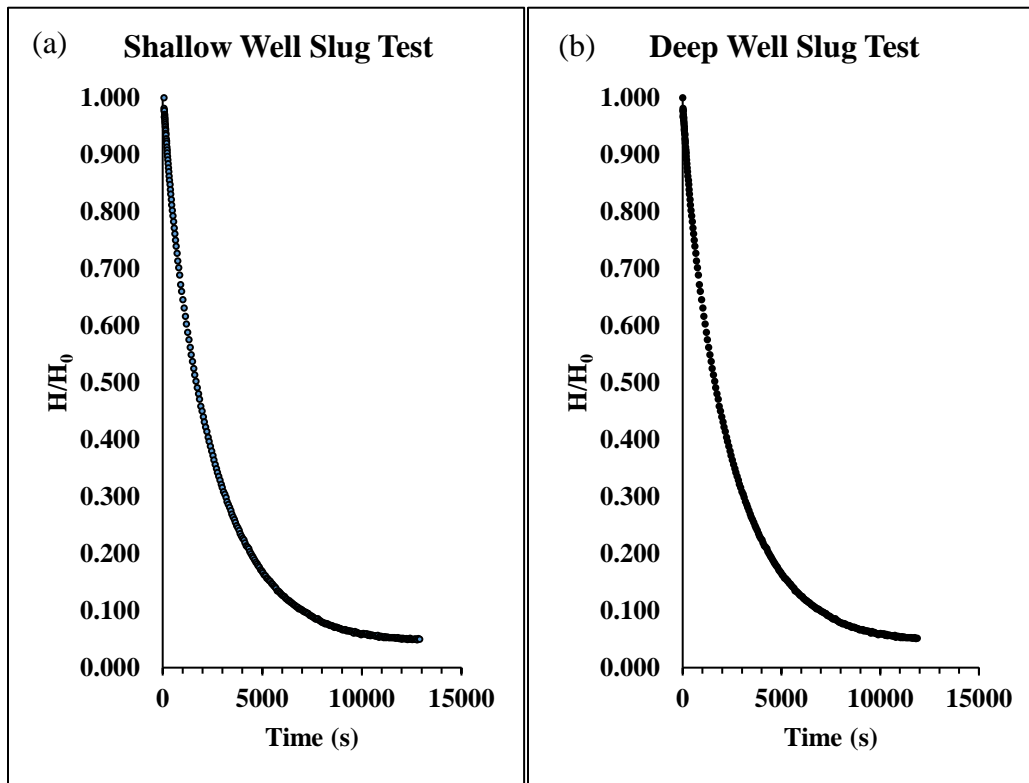


Figure 4 – Change in head over time illustrating the recovery of the (a) shallow ($K=1.98 \times 10^{-06} \text{ m}\cdot\text{s}^{-1}$) and (b) deep wells ($K=1.17 \times 10^{-06}$) during slug tests to determine hydraulic conductivity for Darcian SGD in Table 1.

Table 1 – Darcian SGD rates calculated by applying the hydraulic conductivities obtained from slug tests above and measured hydraulic gradients.

	Darcian ($\text{cm}\cdot\text{d}^{-1}$)					
	T1-T2	T2-T3	T3-T4	T4-T5	T5-T6	AVG
Shallow	0.45	0.48	0.46	0.47	0.46	0.46
Deep	0.40	0.44	0.42	0.43	0.42	0.42

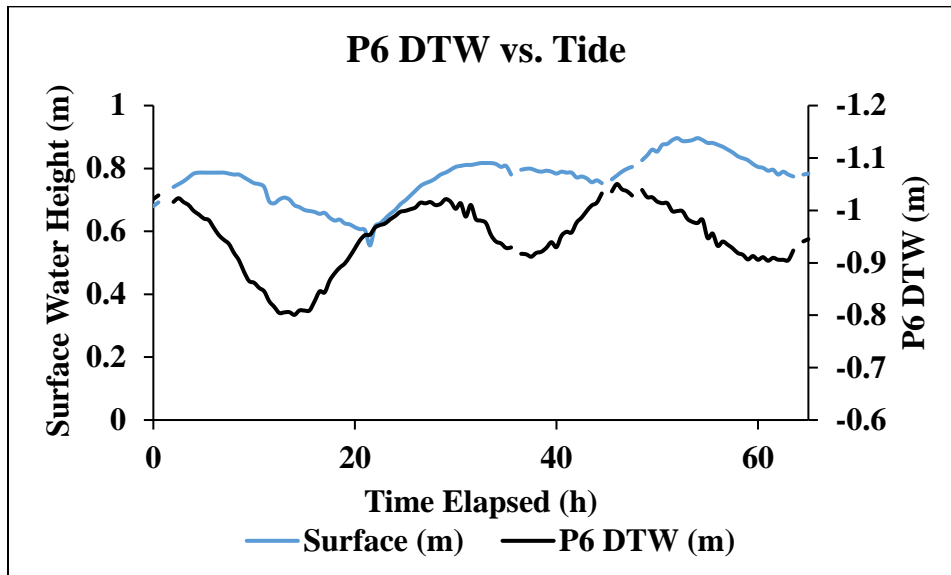


Figure 5 - Surface water height plotted with DTW in P6 measured by pressure transducer over time on secondary axis. There was found to be a six-hour lag correlation between surface water height and P6 DTW - R^2 (0.7984) and p-value (2×10^{-25}).

3.3 Radioisotope SGD Calculations

3.3.1 Time Series ²²²Rn-Derived SGD

As previously mentioned, surface water ²²²Rn was monitored continuously via the platform. The intake was positioned approximately 100 m from shore in 0.95 m of water which fluctuated with small tidal changes. There were three instances where the pump on the platform was found not running due to a lack of solar power. This occurred on 11/15 6:00 am to 10:15 am, 11/16 1:00 am to 9:00 am, and 11/17 11:00 pm to 12:45 am. ²²²Rn activities ranged from 21 Bq·m⁻³ to 274 Bq·m⁻³ (\bar{x} =123 Bq·m⁻³, n=128) (Figure 6). These data were removed from SGD calculations.

3.3.1.1 Porewater and Groundwater Radon Activities

Grab samples for ²²²Rn were collected during all six sampling periods in the shallow well, deep well, P3, and P4. Grab samples were collected for GWW, P1, P2, and P6 during T1, T4, and T6. Activities of ²²²Rn ranged between : 2340 Bq·m⁻³ and 13800 Bq·m⁻³ (\bar{x} =651, n=6) in the shallow well; and 89 Bq·m⁻³ and 9523 Bq·m⁻³ (\bar{x} =3552, n=6) in the deep well; 434 Bq·m⁻³ and 1371 Bq·m⁻³ (\bar{x} =759, n=3) for GWW; 2835 Bq·m⁻³ and 6148 Bq·m⁻³ (\bar{x} =4643, n= 3) for P1; 786 Bq·m⁻³ and 8858 Bq·m⁻³ (\bar{x} =5906, n=3) for P2, 55 Bq·m⁻³ and 3053 Bq·m⁻³ (\bar{x} =1911, n=6) for P3; 366 Bq·m⁻³ to 4465 Bq·m⁻³ (\bar{x} =2542, n=6) for P4, and 59 Bq·m⁻³ and 825 Bq·m⁻³ (\bar{x} =355, n=3) for P6 (Table 2).

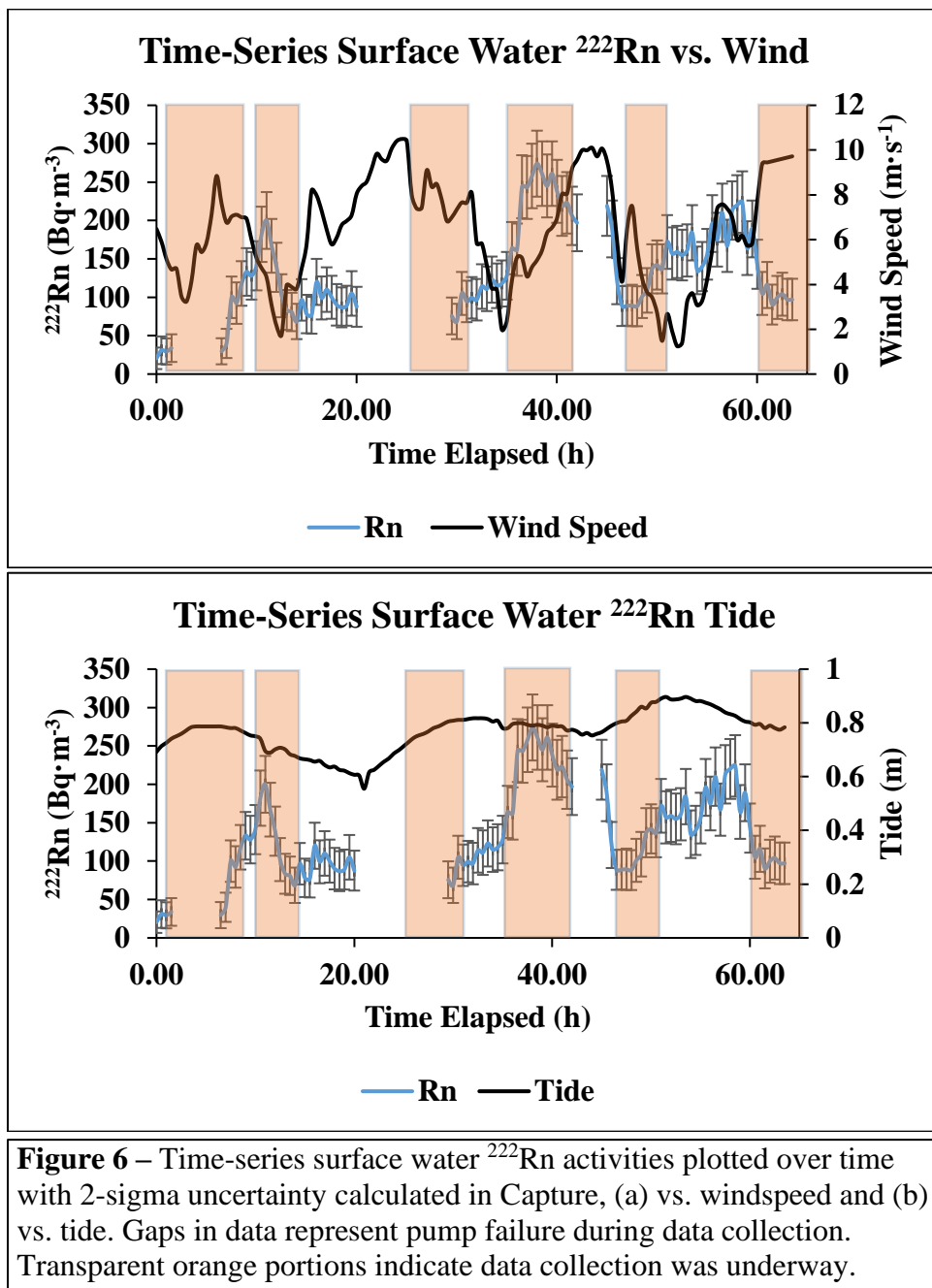


Table 2 – ^{222}Rn endmember activities in $\text{Bq}\cdot\text{m}^{-3}$. Samples were not collected at time steps T2, T3 and T5 from GWW, P1, P2 and P6. Error calculated as 2-sigma uncertainty via Capture.									
^{222}Rn	Shallow	Deep	GWW	P1	P2	P3	P4	P6	Avg. Pore
T1	2698 ± 1525	89 ± 520	1371 ± 1125	2835 ± 1525	8858 ± 2525	3053 ± 1575	3128 ± 1600	825 ± 1000	3739
T2	5573 ± 2075	725 ± 925				2075 ± 1375	2875 ± 1575		2475
T3	13800 ± 3100	9523 ± 2600				2595 ± 1500	4465 ± 1875		3530
T4	7238 ± 2300	7400 ± 2350	434 ± 825	4948 ± 1975	8073 ± 2425	1571 ± 1225	1275 ± 1125	59 ± 585	3185
T5	7423 ± 2325	1753 ± 1300				2120 ± 1375	3145 ± 1650		2633
T6	2340 ± 1475	1825 ± 1300	473 ± 900	6148 ± 2175	787 ± 910	55 ± 505	367 ± 695	181 ± 675	1507
Avg.	6512	3552	759	4643	5906	1911	2542	355	2845

3.3.1.2 SGD Estimates and Endmembers

Previous studies have emphasized both the difficulty and importance of selecting an appropriate endmember in estimating SGD (Burnett and Dulaiova, 2003; Knee et al., 2016; Peterson et al., 2008; Zarroca et al., 2014). The high-resolution spatial sampling technique employed here provided a wide variety of potential endmembers, which increased the likelihood of identifying an endmember representative of the actual source. In this case, five ^{222}Rn endmembers were applied to estimate SGD rates: 1) the average GWW activity ($\bar{x}=759 \text{ Bq}\cdot\text{m}^{-3}$, $n=3$), 2) the average porewater activity ($\bar{x}=2845 \text{ Bq}\cdot\text{m}^{-3}$, $n=21$), 3) the highest activity in the shallow well ($13800 \text{ Bq}\cdot\text{m}^{-3}$), 4) the highest activity in

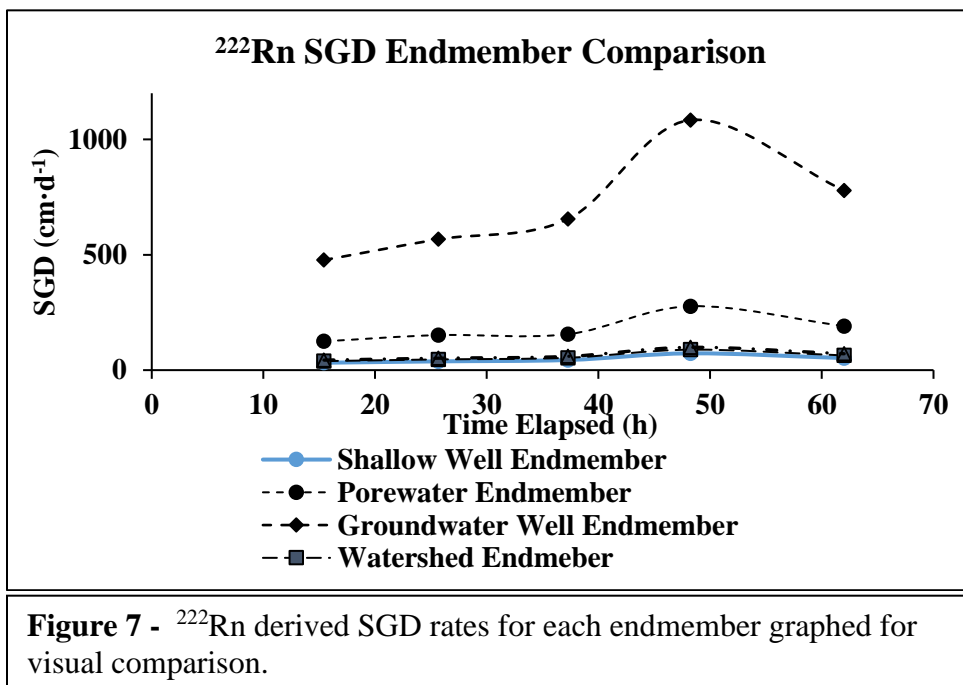
the deep well ($9523 \text{ Bq}\cdot\text{m}^{-3}$), and 5) the average of a number of previously sampled wells located within the watershed ($\bar{x}=11144 \text{ Bq}\cdot\text{m}^{-3}$) (Table 2).

When the average GWW activity, the shoreline endmember, is applied, SGD rates are extremely high for this type of environment. The average porewater activity endmember also result in relatively high rates. The shallow well, deep well, and watershed well average, however, yield the most similar results with magnitudes that agree with other similar studies in the area and in other similar environments. Spalt et al. (2018) presents an overview of available SGD rates in similar environments.

Using the shallow well activity endmember, SGD rates ranged from $36 \text{ cm}\cdot\text{d}^{-1}$ (T1-T2) to $70 \text{ cm}\cdot\text{d}^{-1}$ (T4-T5), and the average SGD rate for the entire sampling event was $49 \text{ cm}\cdot\text{d}^{-1}$. With the deep well activity endmember, SGD rates ranged from $50 \text{ cm}\cdot\text{d}^{-1}$ (T1-T2) to $95 \text{ cm}\cdot\text{d}^{-1}$ (T4-T5), with an average SGD rate of $67 \text{ cm}\cdot\text{d}^{-1}$. It is worth nothing that the lowest SGD rate was estimated at T1 at the highest high tide while the highest rate at T4 at the lowest low tide during the sampling period (Table 3, Figure 7).

Table 3 – ^{222}Rn derived SGD rates for each endmember.						
Shallow Well Endmember						
Timestep	T1-T2	T2-T3	T3-T4	T4-T5	T5-T6	T1-T6
SGD ($\text{cm}\cdot\text{d}^{-1}$)	36	40	48	70	52	47
STDEV	14	4	15	18	11	19
Average Timestep Porewater Endmember						
Timestep	T1-T2	T2-T3	T3-T4	T4-T5	T5-T6	T1-T6
SGD ($\text{cm}\cdot\text{d}^{-1}$)	142	158	171	266	190	175
STDEV	53	17	52	69	39	70
Groundwater Well Endmember (GWW)						
Timestep	T1-T2	T2-T3	T3-T4	T4-T5	T5-T6	T1-T6

SGD (cm·d⁻¹)	543	591	719	1040	778	695
STDEV	202	63	220	272	160	279
Watershed Endmember						
Timestep	T1-T2	T2-T3	T3-T4	T4-T5	T5-T6	T1-T6
SGD (cm·d⁻¹)	44	48	59	85	64	57
STDEV	17	5	18	22	13	23
Deep Well Endmember						
Timestep	T1-T2	T2-T3	T3-T4	T4-T5	T5-T6	T1-T6
SGD (cm·d⁻¹)	50	54	66	95	71	63
STDEV	18	6	20	25	15	26



3.3.2 Time Series ²²³Ra, ²²⁴Ra, and ²²⁶Ra Derived SGD

3.3.2.1 Ra Endmember Activities

The established sampling procedure provided a broad spectrum of endmembers for evaluation of SGD. Activities of the ²²³Ra endmember proved to be consistent across both

spatial and temporal domains, with notable outliers (i.e., higher than average) in P2 at T1 (1659 dpm·m⁻³) and P3 at T4 (1568 dpm·m⁻³) (Table 4). The deep well peaks during T5 and T6 (2625 dpm·m⁻³ and 2016 dpm·m⁻³) but that can be attributed to a hysteresis effect associated with the drastic increase in specific conductance (SPC) observed during previous timesteps from 38486 $\mu\text{S}\cdot\text{cm}^{-1}$ at T1 to 58146 $\mu\text{S}\cdot\text{cm}^{-1}$ through T6. Both modeled and measured SPC data were plotted against ²²³Ra activities. Modeled data showed no correlation ($R^2=0.0081$, p-value=0.9715, n=21) whereas measured data suggests a poor correlation ($R^2=0.2376$, p-value=0.2984, n=21) (Figure 8). Similar trends are reflected in the ²²⁴Ra as measured activities in the deep well increase from 179 dpm·m⁻³ during T1 to 21843 dpm·m⁻³ during T5. Porewater ²²⁴Ra activities remained steady throughout with the exception of P2 whose average activity was more than twice the other three piezometers (13835 dpm·m⁻³) (Table 5). Running the same regression on the ²²⁴Ra activities produces no correlation with the modeled SPC, ²²⁴Ra ($R^2=0.069$, p-value=0.766, n=21) but does show a significant relationship with measured SPC ($R^2=0.7294$, p-value=0.0001, n=21) (Figure 9). Lastly, ²²⁶Ra activities were an order of magnitude higher in the deep well and GWW compared to the surface water, likely due to more mixing and shorter residence times at the surface (Table 6).

Table 4 – ^{223}Ra endmember activities ($\text{dpm}\cdot\text{m}^{-3}$) and associated 10% measurement error.

^{223}Ra	Surface	Shallow	Deep	GW	P1	P2	P3	P4	P6	Avg. Pore
T1	56 ± 6	220 ± 20	34 ± 34	9 ± 1	454 ± 45	1659 ± 166	426 ± 43	415 ± 42	310 ± 31	653
T2	144 ± 14	397 ± 40	992 ± 99				379 ± 38	291 ± 29		335
T3	45 ± 5	338 ± 33	107 ± 11				432 ± 43	336 ± 34		384
T4	95 ± 10	462 ± 46	972 ± 97	7 ± 1	407 ± 41	168 ± 17	1568 ± 157	421 ± 42	259 ± 26	565
T5	84 ± 8	407 ± 41	2625 ± 263				258 ± 26	555 ± 56		406
T6	85 ± 9	538 ± 54	2016 ± 202	18 ± 2	321 ± 32	993 ± 99	330 ± 33	403 ± 40	133 ± 13	436
AVG	85	394	1124	11	394	940	566	403	234	507

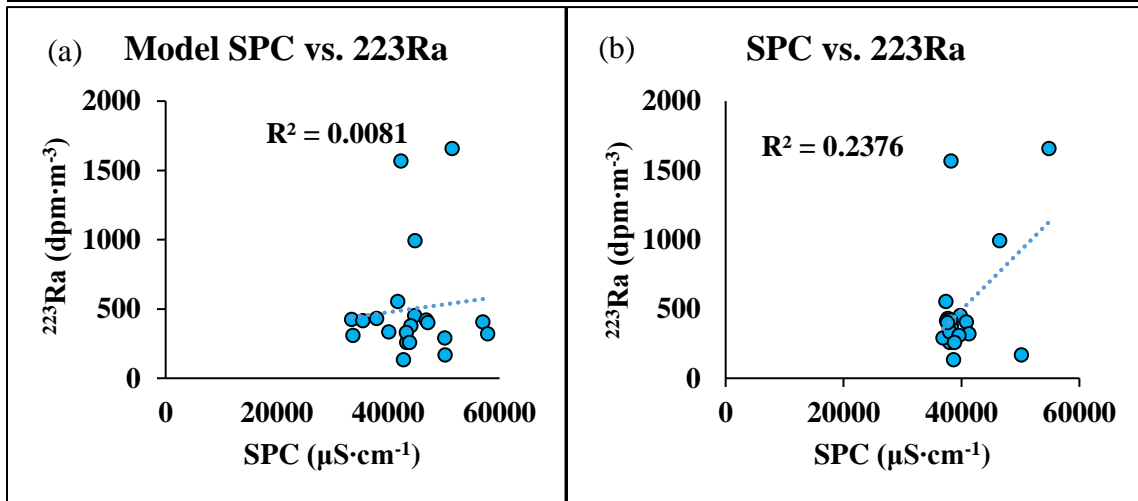


Figure 8 - (a) modeled pore conductivities graphed vs. ^{223}Ra ($R^2=0.0081$, p-value=0.9715, n=21) and (b) measured pore conductivities graphed vs. ^{223}Ra ($R^2=0.2376$, p-value=0.2984, n=21).

Table 5 – ^{224}Ra endmember activities ($\text{dpm}\cdot\text{m}^{-3}$) and associated 10% measurement error.

^{224}Ra	Surface	Shallow	Deep	GW	P1	P2	P3	P4	P6	Avg. Pore
T1	682 ± 68	1294 ± 129	179 ± 18	407 ± 41	5730 ± 573	14741 ± 1474	6804 ± 680	7664 ± 766	6305 ± 631	8249
T2	1635 ± 164	2855 ± 286	170 ± 17				6469 ± 647	5845 ± 585		6157
T3	600 ± 60	2988 ± 299	5498 ± 550				6398 ± 640	6454 ± 645		6426
T4	1465 ± 147	3956 ± 396	7633 ± 763	179 ± 18	6681 ± 668	13707 ± 1371	7138 ± 714	8043 ± 804	5451 ± 545	8204
T5	1059 ± 106	3033 ± 303	21843 ± 2184				6859 ± 686	7945 ± 795		7402
T6	1272 ± 127	4819 ± 482	18335 ± 1834				6472 ± 647	7789 ± 779	2567 ± 257	7271
AVG	1119	3158	8943	248	6293	13835	6690	7290	4774	7776

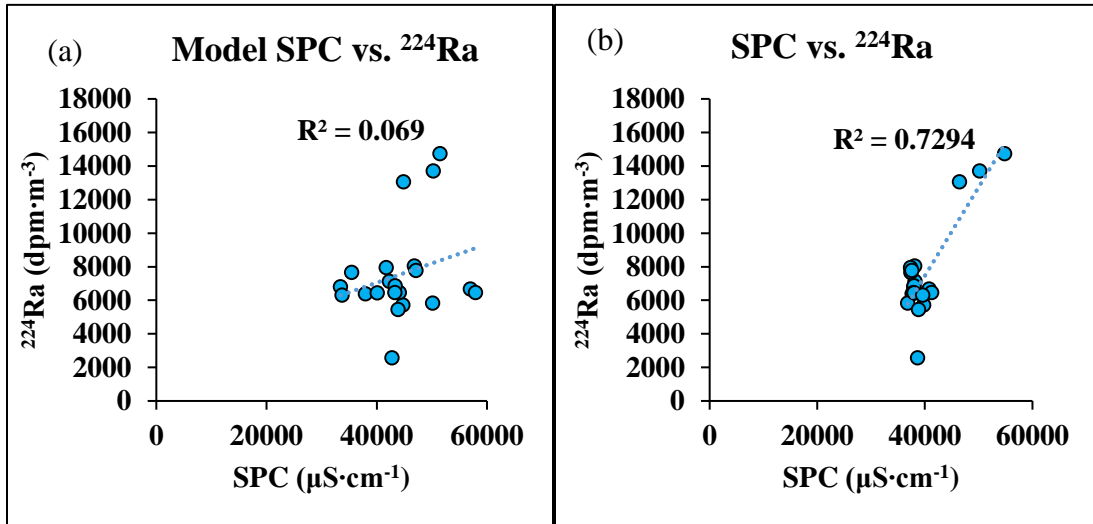


Figure 9 – (a) modeled pore conductivities graphed vs. ^{224}Ra ($R^2=0.069$, p-value=0.766, n=21) and (b) measured pore conductivities graphed vs. ^{224}Ra ($R^2=0.7294$, p-value=0.0001, n=21).

Table 6 – ^{226}Ra endmember activities ($\text{dpm}\cdot\text{m}^{-3}$) and associated 10% measurement error.

^{226}Ra	Surface	Deep	GWW
T1	276±28	3615±362	1206±121
T2	334±33	8834±883	
T3	145±15	6415±642	
T4	350±35	3055±306	1140±114
T5	359±36	6353±635	
T6	397±40	5120±512	8572±857
AVG	310	5565	3639

3.3.2.2 SGD Estimates

Radium-derived SGD rates were estimated similar to ^{222}Rn . SGD rates were derived using the ^{223}Ra , ^{224}Ra , and ^{226}Ra surface water measurements and associated endmembers. However, ^{226}Ra estimates are only available for the deep well and GWW endmembers. One notable difference in performing SGD calculations between radon and radium methods is that individual radium endmember activities were applied to each timestep as opposed to the mean and range values used for ^{222}Rn (Table 2, 3). More specifically, the radium endmembers were applied with a delay. That is, an endmember from T1 was applied to a surface water measurement from T2 under the assumption that there is a time delay between when that endmember is measured in the subsurface and when it is ultimately brought into solution at the surface. Generally, endmember samples were collected approximately 12 hours prior to the collection of the surface water samples their calculations were associated with. One exception was the T1-T2 calculation whose endmember sample was collected during T1 approximately 6 hours prior to the collection of the surface water samples in T2.

The deep well and GWW endmembers for ^{223}Ra , the deep well endmembers for ^{224}Ra , and the deep well endmember for ^{226}Ra yield fluxes within the range anticipated at the study site (Table 7, 8, 9). All other endmember calculations provide unreasonable estimates of SGD, ranging from one order of magnitude above or below the ^{222}Rn values. Measured activities and subsequent calculations in the deep well, however, do appear to be heavily influenced by changes in salinity, skewing results during T1 and T2.

Table 7 – ^{223}Ra derived SGD rates for each endmember.						
^{223}Ra						
Shallow Well Endmember						
Timestep	T1-T2	T2-T3	T3-T4	T4-T5	T5-T6	T1-T6
SGD ($\text{cm}\cdot\text{d}^{-1}$)	11	2	4	3	4	4
STDEV	0.3	0.1	0.1	0.1	0.1	0.1
Average Porewater Endmember						
Timestep	T1-T2	T2-T3	T3-T4	T4-T5	T5-T6	T1-T6
SGD ($\text{cm}\cdot\text{d}^{-1}$)	6	3	5	3	4	4
STDEV	0.2	0.1	0.1	0.1	0.1	0.1
Groundwater Well Endmember						
Timestep	T1-T2	T2-T3	T3-T4	T4-T5	T5-T6	T1-T6
SGD ($\text{cm}\cdot\text{d}^{-1}$)	163	59	120	165	153	126
STDEV	4	1	3	4	4	3
Deep Well Endmember						
Timestep	T1-T2	T2-T3	T3-T4	T4-T5	T5-T6	T1-T6
SGD ($\text{cm}\cdot\text{d}^{-1}$)	1578	1578	40	42	15	49
STDEV	40	11	1	1	0	1

Table 8 - ²²⁴Ra derived SGD rates for each endmember.						
²²⁴Ra						
Shallow Well Endmember						
Timestep	T1-T2	T2-T3	T3-T4	T4-T5	T5-T6	T1-T6
SGD (cm·d⁻¹)	450	79	198	122	181	183
STDEV	11.4	2.0	5.0	3.1	4.6	4.7
Average Porewater Endmember						
Timestep	T1-T2	T2-T3	T3-T4	T4-T5	T5-T6	T1-T6
SGD (cm·d⁻¹)	4	2	4	3	3	3
STDEV	0.1	0.0	0.1	0.1	0.1	0.1
Groundwater Well Endmember						
Timestep	T1-T2	T2-T3	T3-T4	T4-T5	T5-T6	T1-T6
SGD (cm·d⁻¹)	39	15	39	73	95	39
STDEV	1	0	1	2	2	1
Deep Well Endmember						
Timestep	T1-T2	T2-T3	T3-T4	T4-T5	T5-T6	T1-T6
SGD (cm·d⁻¹)	3260	1325	107	63	25	80
STDEV	83	34	3	2	1	2

Table 9 - ²²⁶Ra derived SGD rates for each endmember.						
²²⁶Ra						
Groundwater Well Endmember						
Timestep	T1-T2	T2-T3	T3-T4	T4-T5	T5-T6	T1-T6
SGD (cm·d⁻¹)	0.7	0.2	0.9	1	1	0.8
STDEV	0.1	0.0	0.1	0.1	0.1	0.1
Deep Well Endmember						
Timestep	T1-T2	T2-T3	T3-T4	T4-T5	T5-T6	T1-T6
SGD (cm·d⁻¹)	27	4	19	48	24	21
STDEV	0.8	0.3	0.1	1	0.6	0.5

3.4 Time-Series Electrical Resistivity Tomography (ERT) SGD Calculations

3.4.1 Model Accuracy Evaluation

Pore fluid SPC values measured in-situ during the survey were compared to those calculated using both Archie's Law and the Waxman-Smiths equations via models produced

by the smooth, DLS, and robust inversions, in order to determine the most accurate workflow to proceed with through SGD calculations. Statistical analyses indicate negligible differences between Archie's Law and the Waxman-Smiths equation, but significant differences between each inversion model (Robust Waxman $R^2=0.142$ and $p=0.023$, $n=30$; Robust Archie $R^2=0.142$ and $p=0.023$, $n=30$; Smooth Waxman $R^2=0.0983$ and $p=0.051$, $n=30$; Smooth Archie $R^2=0.0987$ and $p=0.051$, $n=30$; Damped Waxman $R^2=0.0277$ and $p=0.19$, $n=30$; Damped Archie $R^2=0.0277$ and $p=0.19$, $n=30$) (Figure 10, Table 10). The DLS model proved to be the least accurate, producing the lowest correlation to observed conductivities and highest MAE (Figure 10 f and g, Table 10). The smooth inversion performed relatively better (Figure 10 c and d, Table 10), but the robust inversion was objectively the most effective at modeling conductivities (Figure 10 a and b, Table 10). As such, the robust inversion model was used to evaluate SGD.

Table 10 – Results of statistical analyses performed in R for each model including mean absolute error, Pearson correlation, linear regression, and nash-sutcliffe efficiency. As labeled, DA (Damped Archie), DW (Damped Waxman), RA (Robust Archie), RA (2) (Robust Archie sans outliers), RW (Robust Waxman), RW (2) (Robust Waxman sans outliers), SA (Smooth								
	DA	DW	RA	RA (2)	RW	RW (2)	SA	SW
Upper (97.5%)	8206	8159	7281	3948	7242	3938	6722	6715
MAE ($\mu\text{S/cm}$)	6533	6581	5468	3338	5535	3353	5324	5268
Lower (2.5%)	5006	5074	4033	2676	3928	2728	3896	3811
Correlation	0.248	0.248	0.415	0.715	0.414	0.715	0.360	0.359
Pearson's-p	0.187	0.187	0.023	0.0001	0.023	0.0001	0.050	0.050
R^2	0.027	0.027	0.142	0.489	0.142	0.488	0.096	0.096
NSE	-2.91	-2.91	-2.12	0.296	-2.12	0.279	-1.72	-1.72

While none of the models produced totally unreasonable results, there were noticeable outliers present. The robust inversion models had difficulty resolving data at P1 (13.6 m (x), 1.0 m (y)) during time steps 3, 4, 5, and 6, as well as data at P4 (56.4 m

(x), 3 m (y)) during time steps 2, 4, and 6. Removing these outliers (> 10% misfit)

significantly enhanced the fit of both the Robust Archie and Waxman models (Figure 11).

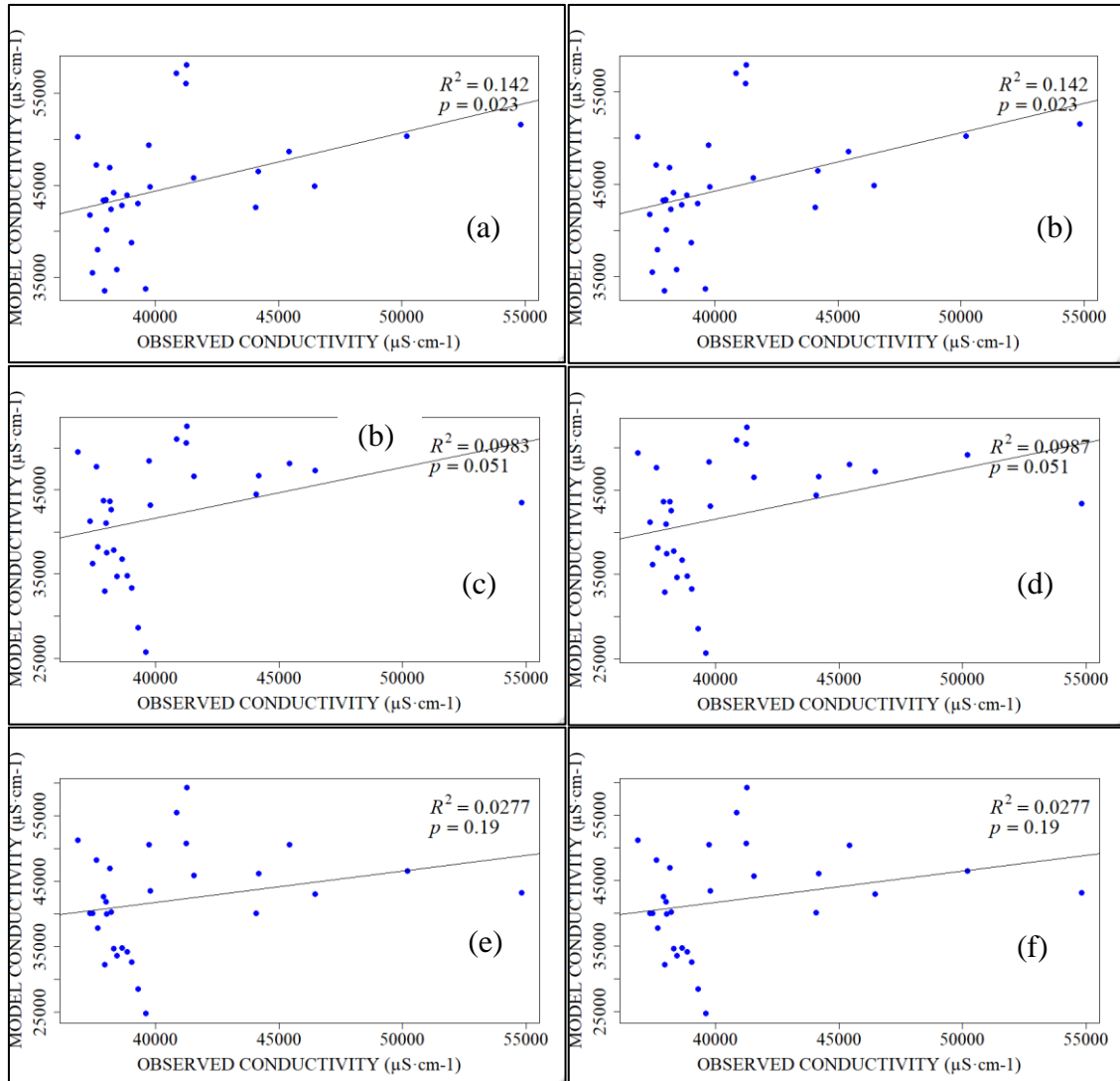
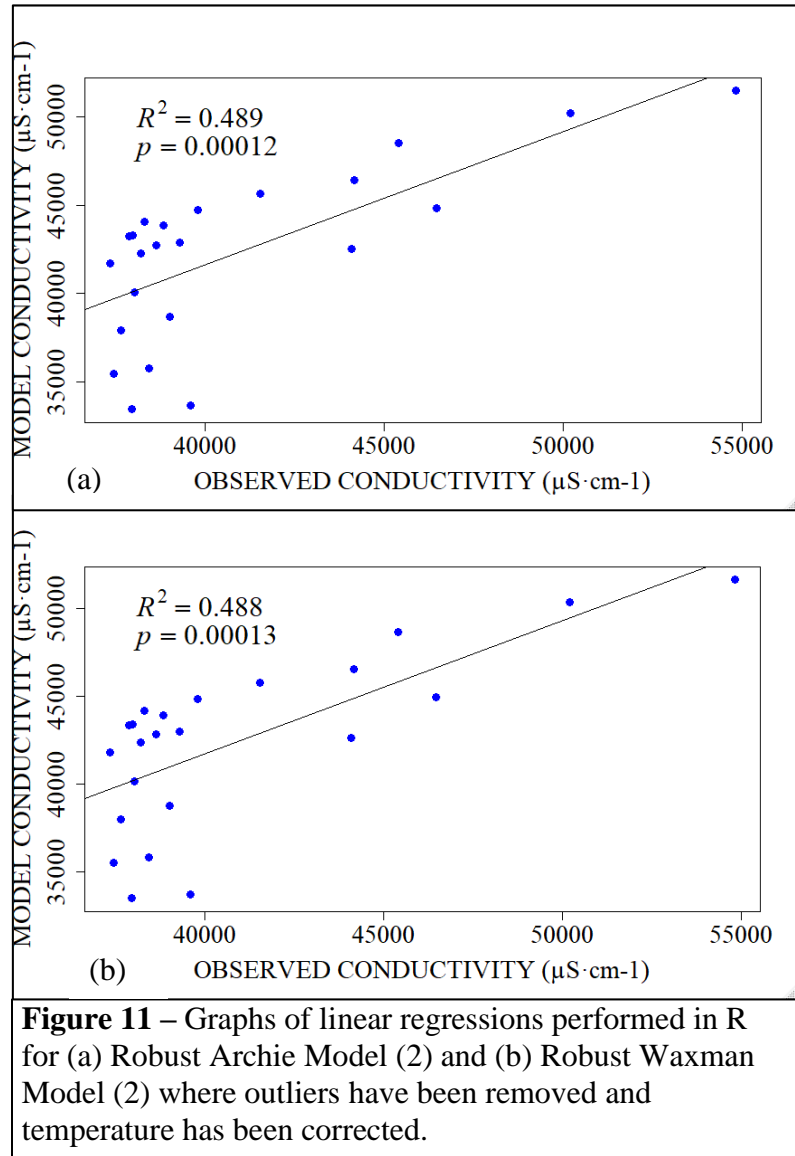


Figure 10 – Graphs of linear regressions performed in R for (a) Robust Waxman Model, (b) Robust Archie Model, (c) Smooth Waxman Model, (d) Smooth Archie Model, (e) Damped Waxman Model, and (f) Damped Archie Model.

As previously mentioned, Onovughe (2016) determined clay minerals to be responsible for inaccurate estimates of fluid content in mixed sand and clay fluid bearing formations as Archie's Law does not take into account the component of bulk conductivity attributed to the surfaces of conductive clays in the ground. If this component is accounted

for in bulk resistivity calculations, the estimated conductivity of the water should theoretically decrease. Thus, the Waxman-Smiths Model, which is a modified extension of Archie's Law, can be applied more accurately to shaly-sands by taking into account the additional measured bulk electrical conductivity created by clays. The technique proved mostly



ineffective as it overestimated fluid conductivities in 73% (22/30) of samples compared to the 70% (21/30) from Archie's Law. Furthermore, the Archie's Law model produced a marginally lower MAE (5468) than the Waxman-Smiths Equation model (5535) (Table 10). In summary, there was no real distinction between the two with respect to the statistics.

Following the determination of an optimal workflow, final inversion models were produced in EarthImager and then Surfer for interpretation (Figure 12, 13, 14, 15).

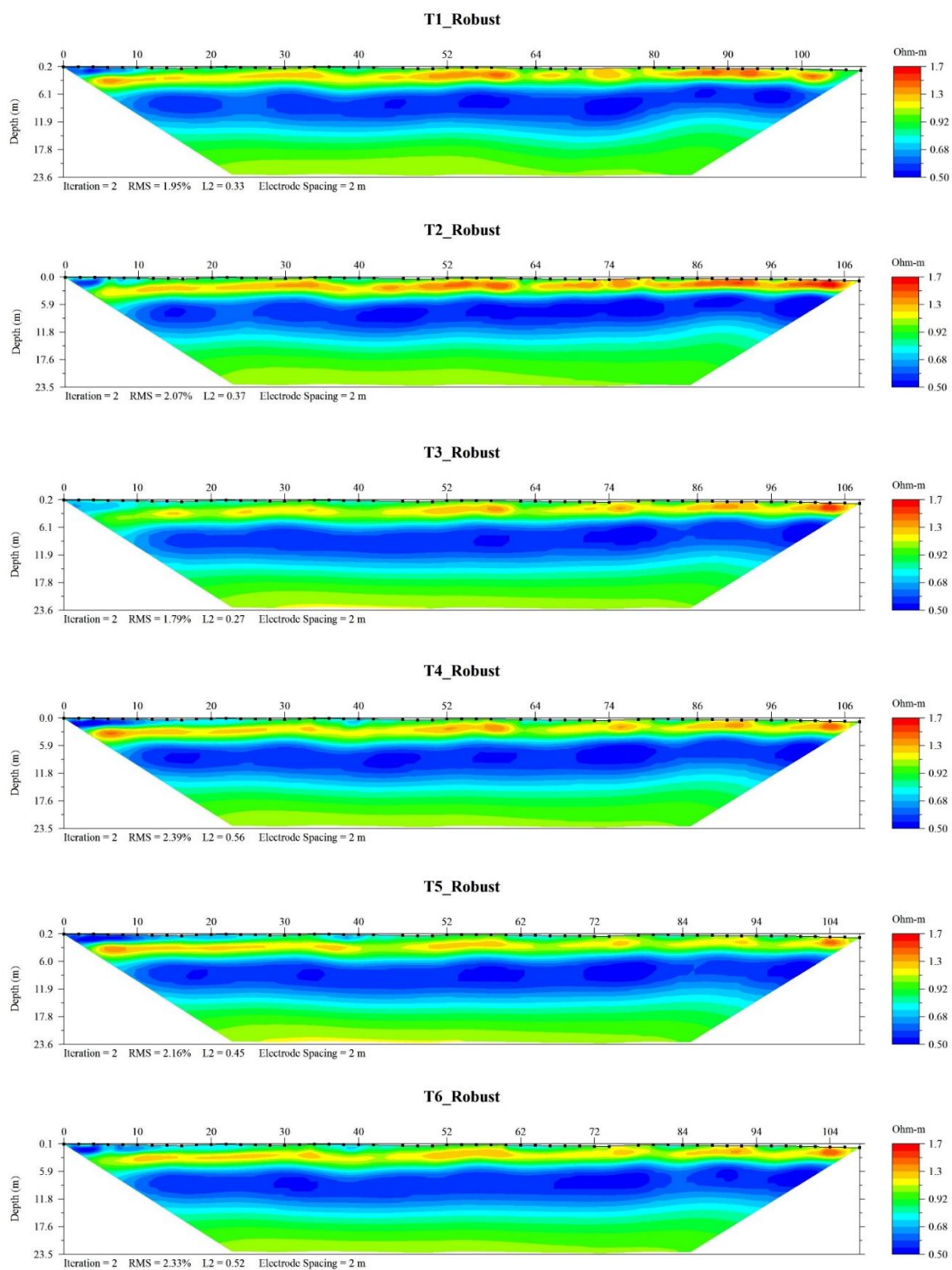


Figure 12 – Electrical resistivity tomograms for each timestep, processed in AGI EarthImager 2D using the robust inversion method (0.5 Ohm-m – 1.7 Ohm -m).

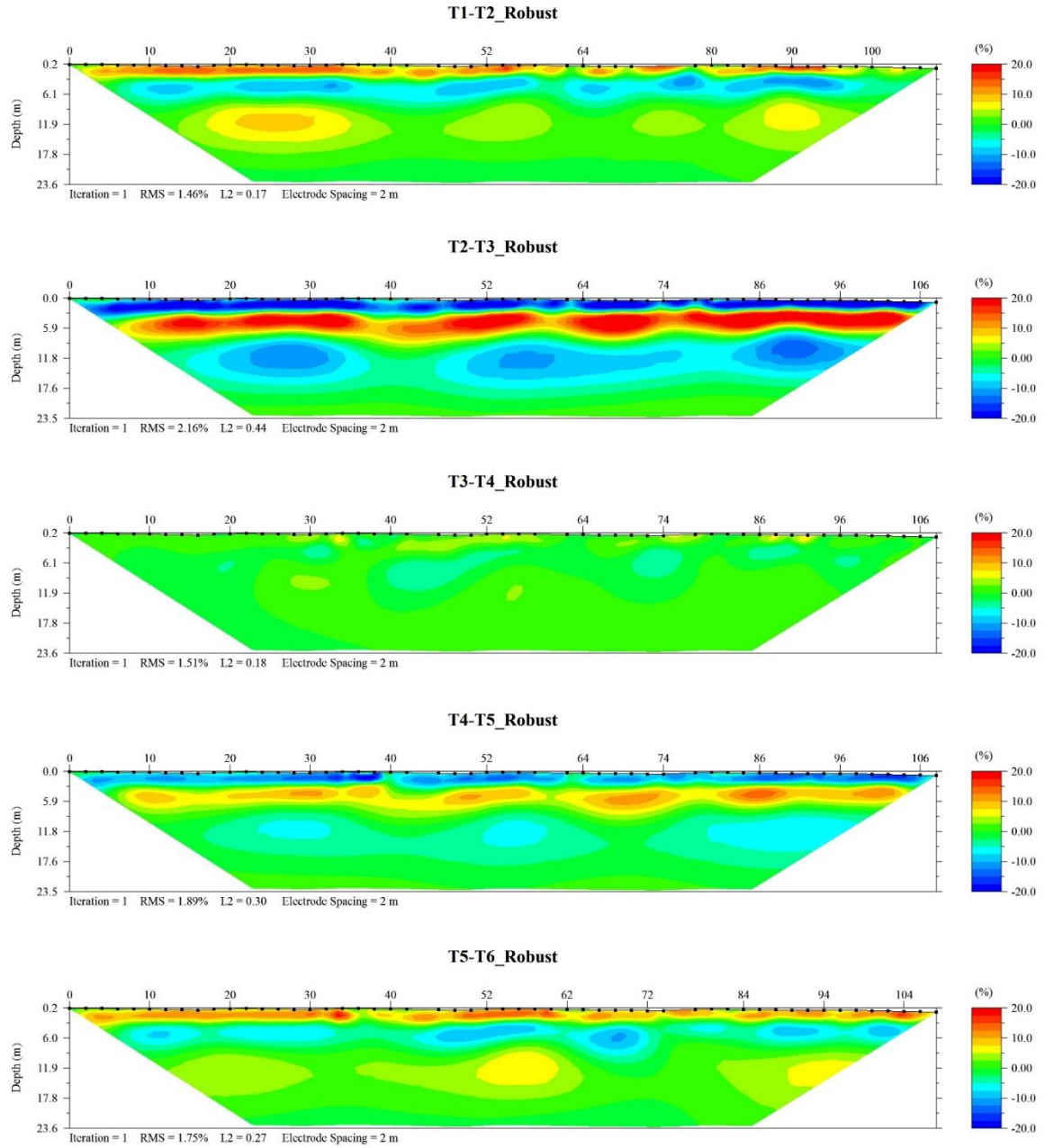


Figure 13 - Electrical resistivity percent difference images processed in EarthImager 2D (-20% - +20%). Calculated as $[(T_{n+1}-T_n)/T_n]*100$.

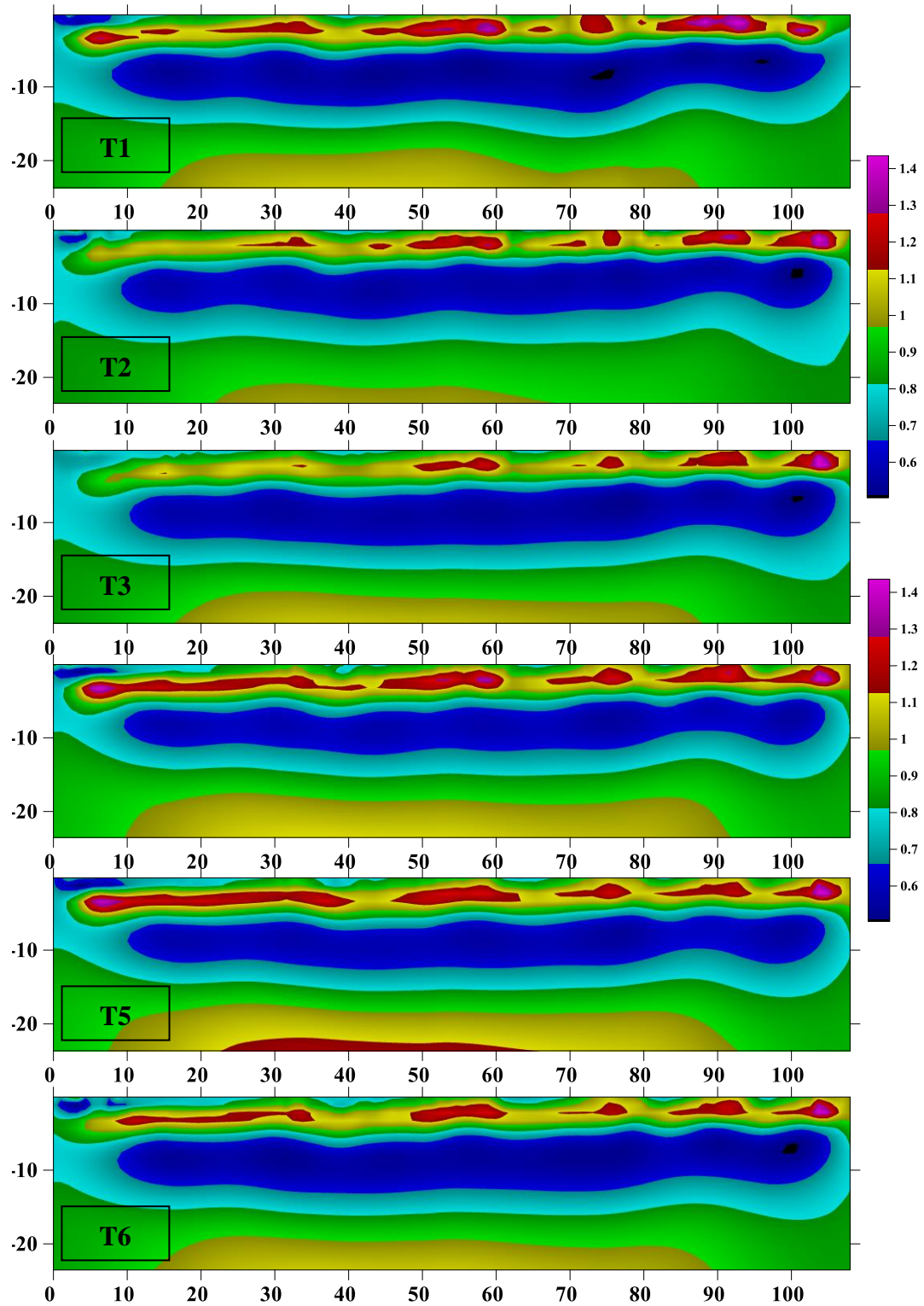


Figure 14 – Color relief electrical resistivity tomograms for each timestep, processed in surfer by kriging grid data exported from EarthImager2D (0.5 Ohm-m – 1.45 Ohm -m).

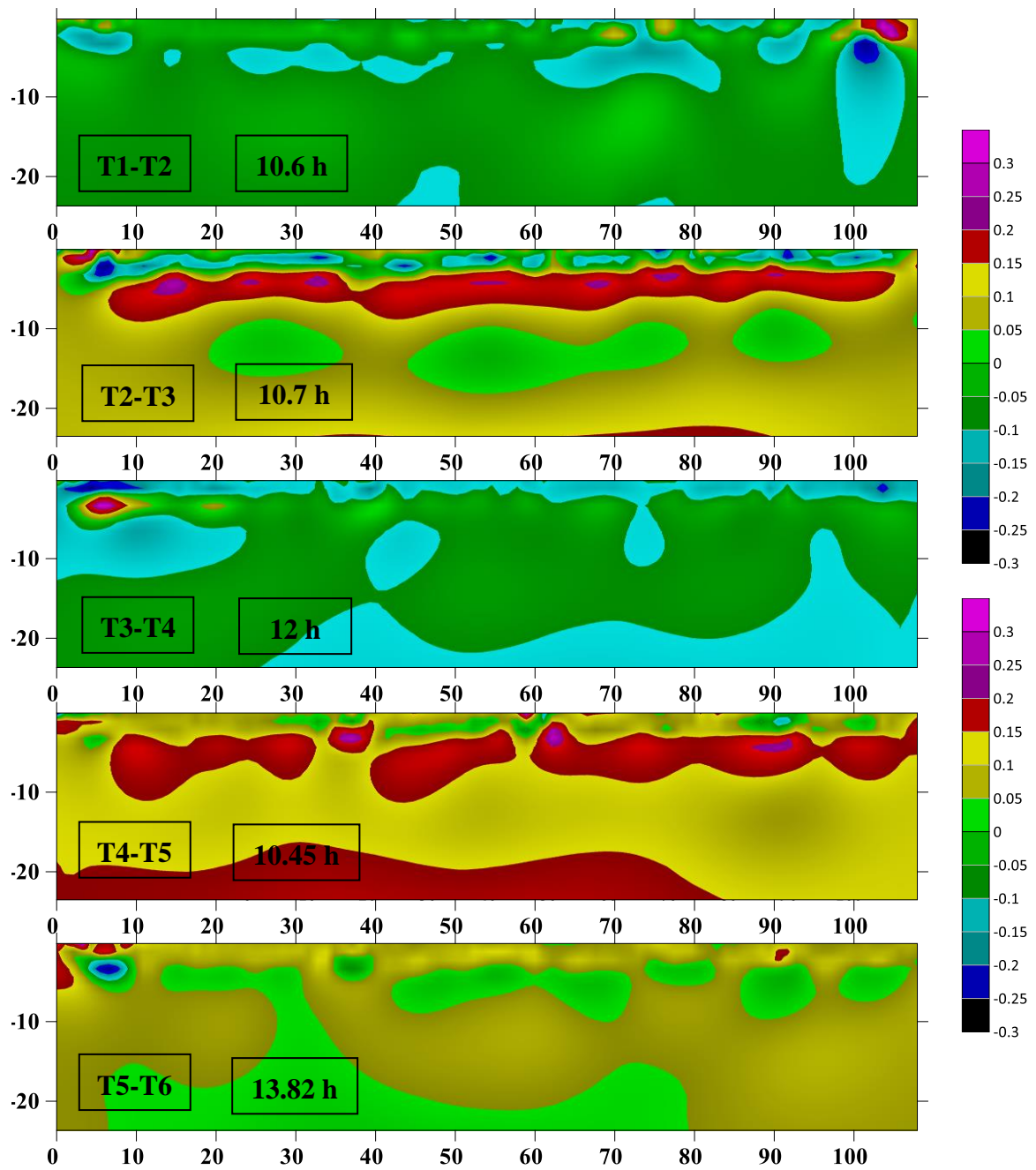


Figure 15 - Color relief electrical difference images, processed in surfer by applying a kriging interpolation on grid data exported from EarthImager2D (-0.3 Ohm-m - +0.3 Ohm-m). Calculated as $T_{n+1} - T_n$. Time elapsed between timesteps labeled on figures.

3.4.2 Archie's Law SGD Estimates

SGD rates calculated according to Archie's Law yielded relatively low values in comparison to the geochemical techniques. While on the same order of magnitude, the estimates overall trend in the opposite direction of the ^{222}Rn measurements (Figure 16, Table 11). Notably, the SGD rates show no relation to the tidal cycle.

3.4.3 Waxman-Smits SGD Estimates

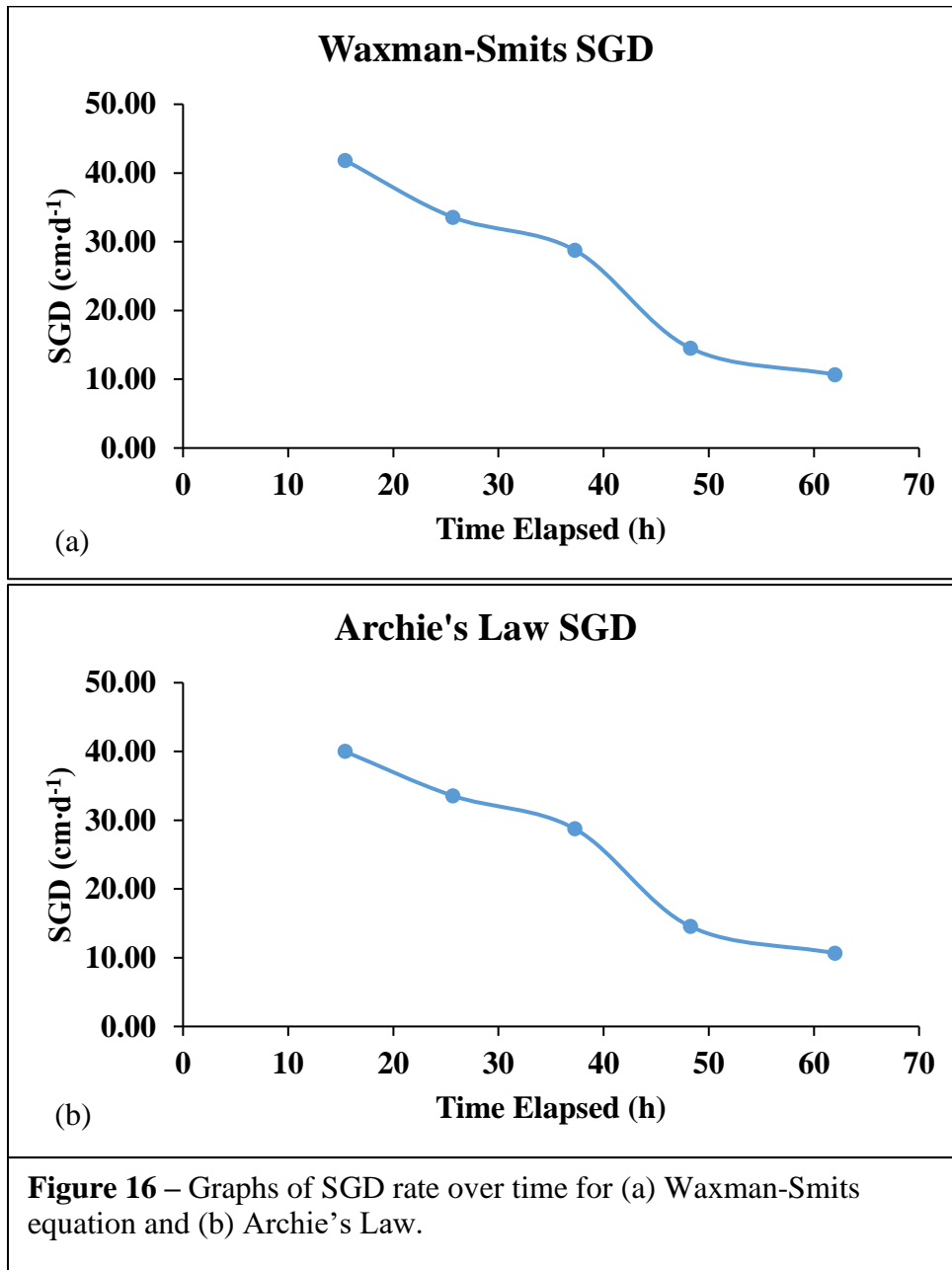
SGD rates calculated with respect to the Waxman-Smits equation were almost identical in trend and magnitude to those from Archie's Law, with only slightly higher rates on average in comparison (Figure 16, Table 11, 12). While it was anticipated that this set of equations would account for the clay component in the bulk conductivity of the subsurface and thus reduce calculated fluid conductivity values, no definite trend was observed as produced values were marginally higher than Archie's Law (Figure 16, Table 12). Again, notably, the SGD rates show no relation to the tidal cycle.

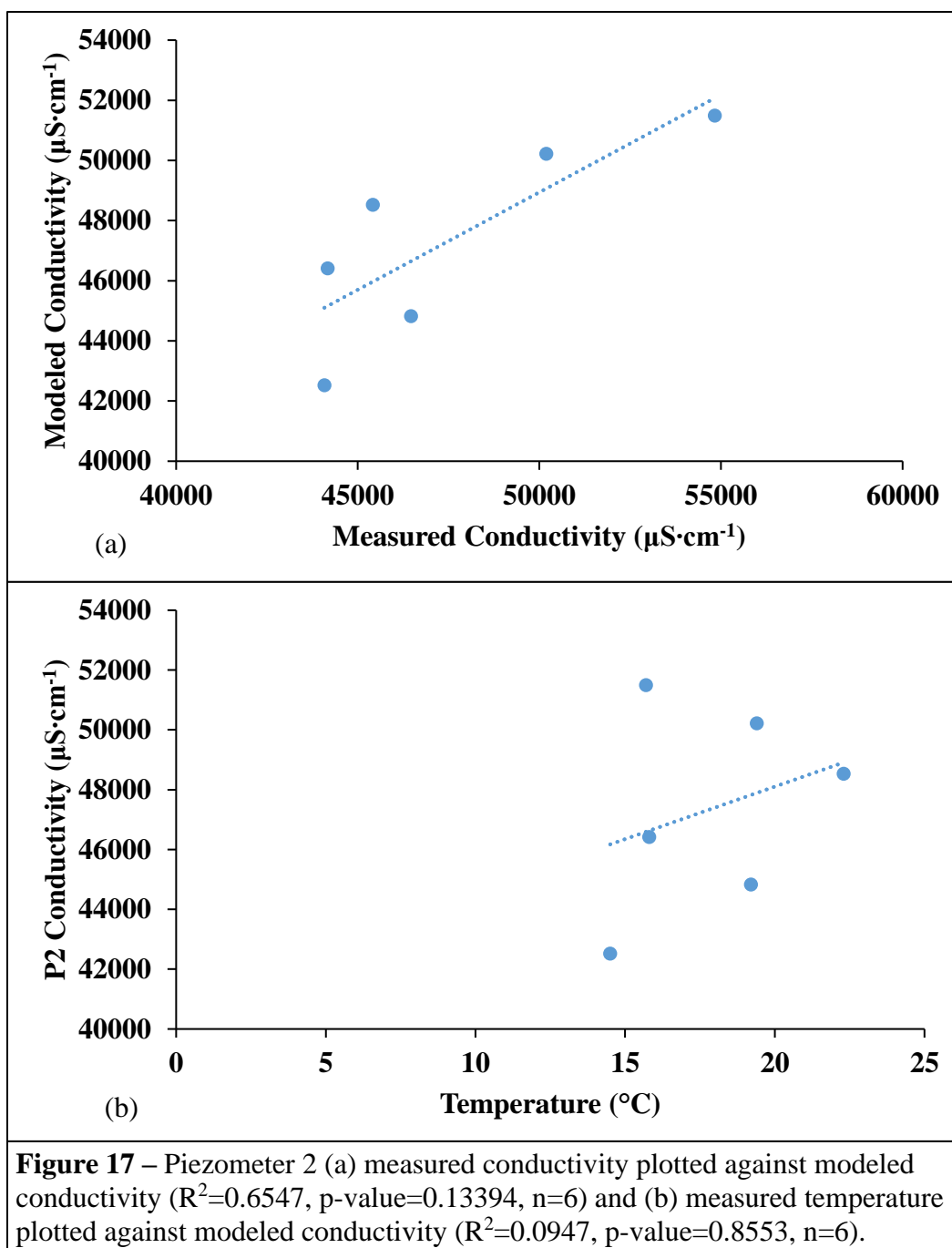
Table 11 – Archie's Law ERT derived SGD rates.

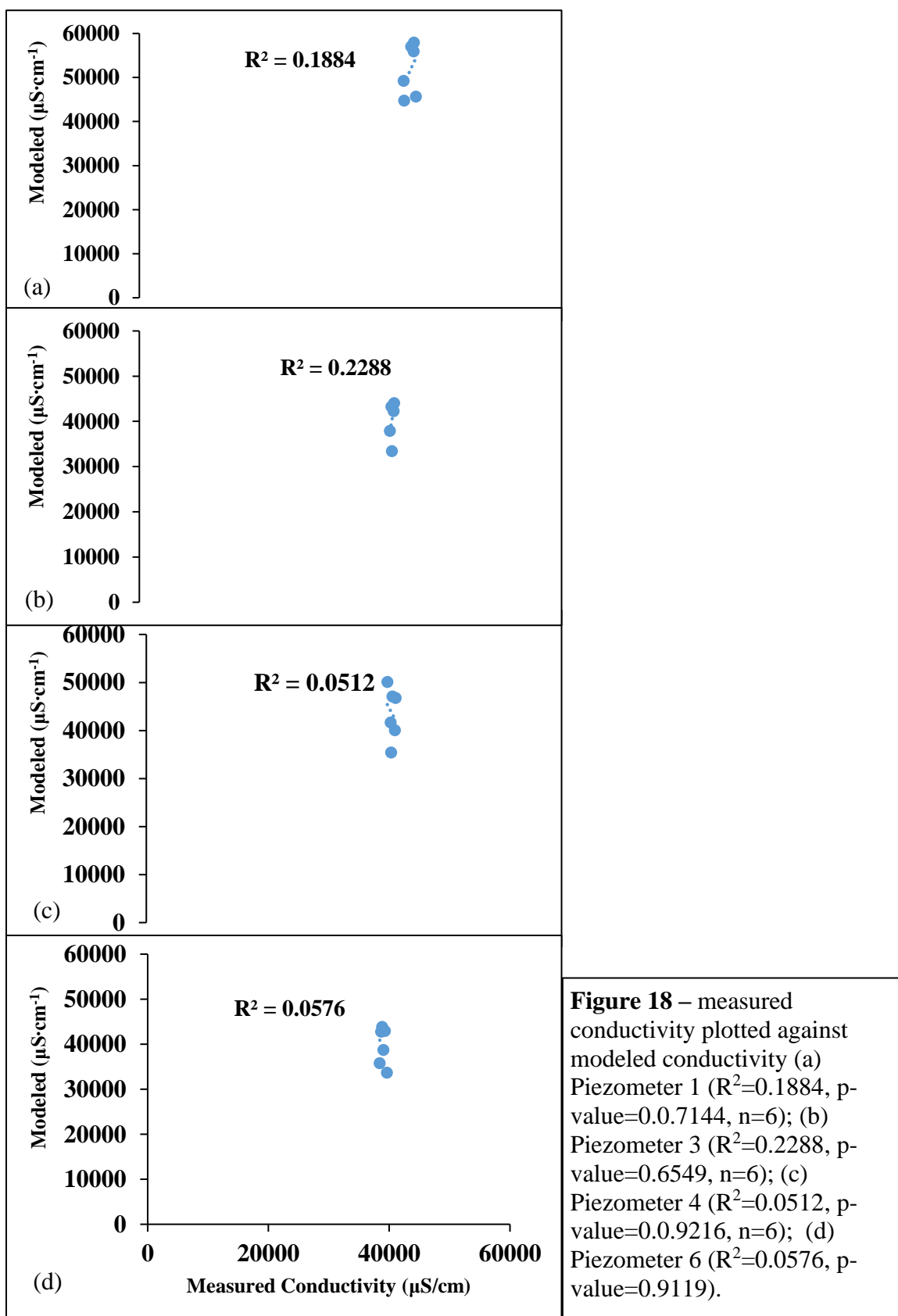
Timestep	T1-T2	T2-T3	T3-T4	T4-T5	T5-T6	T1-T6
SGD (cm·d⁻¹)	40	34	29	15	11	26

Table 12 – Waxman-Smits ERT derived SGD rates.

Timestep	T1-T2	T2-T3	T3-T4	T4-T5	T5-T6	T1-T6
SGD (cm·d⁻¹)	42	34	29	15	11	26







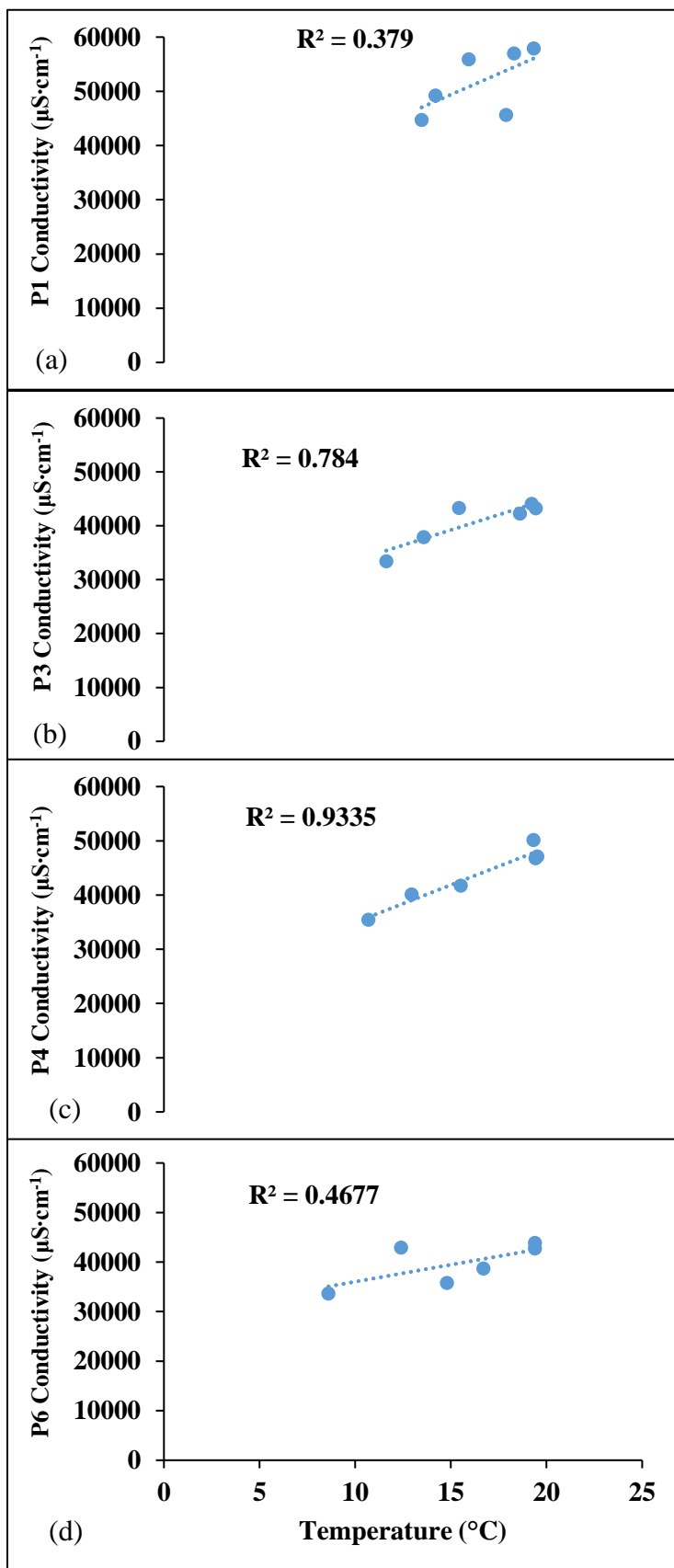
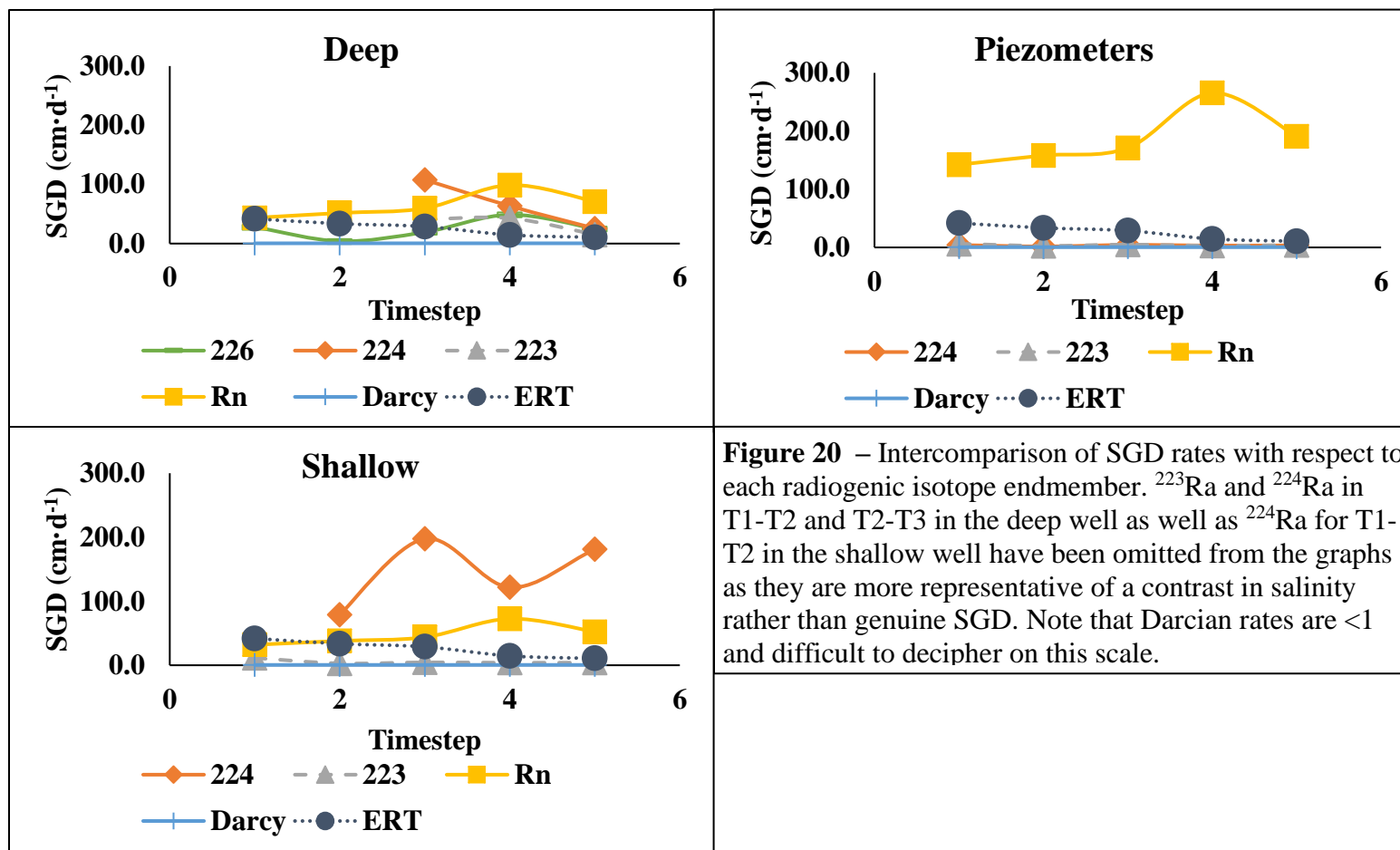


Figure 19 – measured temperature plotted against modeled conductivity (a) Piezometer 1 ($R^2=0.379$, p-value=0.4440, n=6); (b) Piezometer 3 ($R^2=0.784$, p-value=0.0449, n=6); (c) Piezometer 4 ($R^2=0.9335$, p-value=0.002); (d) Piezometer 6 ($R^2=0.4677$, p-value=0.3307).

Table 13 – Recorded water quality parameters, sample depths, collection times, and water levels (AMSL) for every sample throughout the survey.

YSI	T1	P1-1	P2-1	P3-1	P4-1	P6-1	GWW	Deep	Shallow
Temp (°C)	10.7	13.1	15.7	11.3	10.4	8.6	16.1	24.2	22.4
Pressure mmHg	770.4	771.5	771.4	771.1	771	770.4	771.4	770.6	769.4
DO%	193.4	112.6	80.6	83.2	125.2	158.2	146.8	146.6	224.5
DO (mg·L ⁻¹)	18.92	10.12	6.35	7.8	11.78	15.47	13.77	10.66	17.8
SPC (μS·cm ⁻¹)	32230	39788	54832	37954	37450	39601	3975	38486	14854
SAL	20.07	25.38	36.82	24.09	23.66	25.07	2.13	24.51	8.66
pH	7.44	7.33	7.07	7.25	7.23	7.19	7.9	6.76	7.01
ORP	15.9	-182.6	-41.2	-35.41	37	-120.9	-146.9	-122.4	-67.3
Time (h)	1.43	5.05	4.73	4.15	3.58	1.00	5.30	6.97	8.37
Depth (m)	0.68	1.50	3.00	1.50	3.00	2.00	0.75	41.00	19.20
AMSL (m)		0.01	-0.03	0.06	-0.03	-0.03	0.01	0.15	0.21
YSI	T2	P1-2	P2-2	P3-2	P4-2	P6-2	GWW	Deep	Shallow
Temp (°C)	18.4	17.4	22.4	18.7	18.8	16.7	11.8	23.4	19.6
Pressure mmHg	767.3	767.4	767.2	767.1	767.2	767.6	768	768.2	768.2
DO%	180.1	89.2	69.8	73.2	87.3	134.6	129.3	109.1	176.5
DO (mg·L ⁻¹)	14.82	7.32	5.16	5.9	7.05	11.03	13.4	7.68	15.2
SPC (μS·cm ⁻¹)	32828	41549	45415	38300	36850	39025	6629	50210	16572
SAL	20.58	26.69	29.44	24.38	23.39	24.89	3.09	32.94	9.75
pH	7.6	7.25	7.1	7.21	7.16	7.43	7.88	6.69	6.98
ORP	-44.5	-157.1	23.7	-18.6	77.1	-32.6	33.6	-117.8	-86.7
Time (h)	13.08	13.05	12.98	12.92	12.87	13.27	13.95	14.50	15.42
Depth (m)	0.48	1.50	3.00	1.50	3.00	2.00	0.75	41.00	19.20
AMSL (m)		-0.10	0.00	-0.13	-0.03	0.00	0.01	0.32	-0.44
YSI	T3	P1-3	P2-3	P3-3	P4-3	P6-3	GWW	Deep	Shallow
Temp (°C)	13.7	13.8	14.5	13.2	12.6	12.4	15	24	24
Pressure mmHg	768.1	767.9	767.9	767.8	767.5	767.6	768.3	767.5	767.1
DO%	103.9	77.7	86.4	91.6	123.9	112.4	145.3	150.3	73.3
DO (mg/L)	9.37	6.9	7.32	8.23	11.14	10.23	13.93	9.72	5.81
SPC	35027	39723	44080	37660	38028	39302	19419	54365	16879
SAL	22.07	25.32	28.53	23.88	24.12	24.97	11.81	35.99	9.92
pH	7.6	7.45	7.29	7.41	7.34	7.33	7.78	6.61	6.98
ORP	-65.4	-146.3	-48.7	-66.3	32.6	-42.1	-6	-73.9	-84.5
Time (h)	26.60	26.43	26.27	25.95	25.67	25.55	27.10	31.00	31.67
Depth (m)	0.62	1.50	3.00	1.50	3.00	2.00	0.75	41.00	19.20
AMSL (m)		-0.15	-0.03	-0.30	-0.03	0.00	0.01	0.08	-0.54

YSI	T4	P1-4	P2-4	P3-4	P4-4	P6-4	GWW	Deep	Shallow
Temp (°C)	18.7	17.8	19.4	18.1	18.9	19.4	14.5	22.4	21.7
Pressure mmHg	765.5	765.5	765.4	765.2	765.2	764.9	765.6	765.3	765.3
DO%	115.3	50.8	56.6	87.1	104.9	136.2	89.3	77.6	98.1
DO (mg·L ⁻¹)	9.65	4.1	4.22	1.08	8.34	10.83	9.05	5.34	8.1
SPC (μS·cm ⁻¹)	35062	40841	50189	38215	38145	38839	723	55172	16190
SAL	22.11	26.15	32.95	24.36	24.28	24.76	0.34	36.7	9.53
pH	7.69	7.34	7.12	7.4	7.33	7.63	8.04	6.61	7.02
ORP	-73.4	-181.8	2.5	-50.6	5.7	21.5	-39.4	-37.6	-80.1
Time (h)	38.65	38.58	38.28	37.82	37.27	35.68	39.03	40.82	41.73
Depth (m)	0.55	1.50	3.00	1.50	3.00	2.00	0.75	4.91	5.23
AMSL (m)		-0.25	-0.08	-0.08	0.01	0.00	0.01	16.09	17.16
YSI	T5	P1-5	P2-5	P3-5	P4-5	P6-5	GWW	Deep	Shallow
Temp (°C)	15.4	15.5	15.8	15	15.1	14.8	19.9	18.6	23.7
Pressure mmHg	764.3	764	763.9	764.1	764.2	764.4	764.3	764.5	764.8
DO%	85.2	68	54.1	77.2	66.4	134.8	81.8	118.7	168.3
DO (mg·L ⁻¹)	7.49	5.56	4.38	6.55	5.81	11.25	7.36	8.57	12.62
SPC (μS·cm ⁻¹)	34821	41236	44168	37990	37348	38430	1126	55697	16514
SAL	21.99	26.38	28.57	24.16	23.7	24.6	0.55	37.11	9.69
pH	7.58	7.34	7.25	7.38	7.35	7.44	8.23	6.68	6.93
ORP	-53	-142.4	19	-19.1	-3.4	-48.9	-61.8	-17.9	-62.1
Time (h)	49.35	49.13	49.03	48.60	48.25	48.03	49.40	50.67	51.43
Depth (m)	0.65	1.50	3.00	1.50	3.00	2.00	0.75	41.00	19.20
AMSL (m)		-0.18	-0.03	-0.34	0.00	0.00	0.01	0.72	-0.05
YSI	T6	P1-6	P2-6	P3-6	P4-6	P6-6	GWW	Deep	Shallow
Temp (°C)	18.5	18.8	19.2	18.9	19	19.4	20.5	23.5	23.9
Pressure mmHg	763.9	763.7	763.5	763.3	763.4	763.2	763	762.5	762.9
DO%	103.8	44.1	40.2	48.4	64	68.6	105.4	53.2	40.2
DO (mg·L ⁻¹)	8.55	3.45	3	4.05	51.6	5.42	9.85	3.43	3.18
SPC (μS·cm ⁻¹)	33637	41267	46465	37886	37615	38650	744	58145	18271
SAL	21.17	26.5	30.23	24.13	23.92	24.64	0.41	38.87	10.85
pH	7.58	7.33	7.18	7.4	7.32	7.47	7.83	6.6	6.91
ORP	15.3	-79.4	26.3	-8	25.2	-2.5	11.3	11.7	1.8
Time (h)	65.65	65.75	65.50	64.75	64.28	63.75	63.17	61.67	62.70
Depth (m)	0.60	1.50	3.00	1.50	3.00	2.00	0.75	41.00	19.20
AMSL (m)		-0.06	-0.01	0.05	-0.03	0.00	0.01	0.04	-0.58



4. Discussion

In evaluating the reliability of the electrical resistivity tomography method in this context, three things are considered: error in the model specific to this environment, identifying and correcting for potential artifacts, and optimizing final SGD calculations. Ultimately this was accomplished by considering the proximity of modeled fluid conductivity values to constrained measurements and the accuracy of the final SGD calculations with respect to the radiogenic isotope methods and hydrodynamic model.

The field constraints employed during the ERT survey proved valuable in evaluating model error in this environment. By comparing modeled vs. measured conductivity measurements, the robust inversion was determined to be most effective when processing these data. While recorded resistivity values were extremely low given the hyper-conductive nature of the subsurface, this was accounted for during processing by enabling the conductive earth setting where the model is inverted. If the conductive earth setting was not enabled, the model would likely produce an inaccurate depiction of the subsurface (AGI, 2008).

While measured conductivity values provided strong constraints in order to determine inversion type, survey geometry was not evaluated for accuracy in this environment. As previously mentioned, many studies have used the 2D dipole-dipole method due to the enhanced horizontal resolution across the profile. With respect to survey geometry, the pole-pole method would be worth investigating to achieve stronger signal strength and depth of penetration at the cost of lower model resolution, though it has not yet been employed. Lastly, the pole-dipole array has been shown to be a compromise

between the pole-pole array (with good signal strength) and the dipole-dipole array (high model resolution) and has been successfully used recently in studying SGD (Carretero et al., 2019).

Following processing, the kriging interpolation performed in Surfer was used as, according to the Golden Software support manual, it is most useful when there is a spatially correlated distance or directional bias in the data, and it is often used in soil science and geology applications. The nearest neighbor method would have been useful as it is commonly applied to regularly spaced data with some missing points, but it does not account for anisotropy, a key characteristic of the subsurface of the study site. Furthermore, the natural neighbor method is best applied to data sets with dense data in some areas and sparse data in others. Lastly, the triangulations with linear interpolation method has been shown to be most adequate for large scale topographic data sets. The premise of these methods would lead to inaccurate characterizations of the subsurface and thus poor estimations of SGD (Golden Software Support).

One challenge encountered while evaluating modeled vs. measured conductivity data was dissecting the different domains in which data were collected (time, distance, and depth). Notably, when these data were compared at each individual piezometer (distance), data at P2 produced objectivity the most accurate values. The modeled conductivities were subsequently plotted against measured temperatures to determine the relationship between variables. Linear regression analyses indicated that all modeled conductivities had a significant positive correlation with temperature with the exception of P2 (Figure, 17, 18, 19). This relationship indicates changes in modeled fluid conductivity were influenced

considerably by changes in temperature. As temperature was accounted for when fluid conductivity was derived from bulk conductivity, this suggests that temperature was poorly constrained in the field. Hayley (2010) used forward modeling to develop a time-lapse temperature correction in response to the introduction of significant error to the model related to changes in temperature. It was found that an alternative temperature correction method that corrects ERT data for temperature as opposed to inversion models was the most effective approach to eliminate anomalies associated with inversion. An open source 2.5D forward modeling and inversion code described in (Pidlisecky and Knight, 2008) was applied here which allowed the researchers to correct for temperature prior to inversion. In EarthImager2D, temperature constraints are restricted to the surface water column. While Hayley (2010) statistical analyses claim that the subsurface temperature must be accounted for as well in order to produce a reliable model.

A contrast in reliance of electrical conductivity on temperature would suggest that source water at P2 is from a different source than that at the other piezometers, and the geochemical parameters support this distinction. Average measured conductivity at P2 was $47525 \mu\text{S}\cdot\text{cm}^{-1}$ compared to $38821 \mu\text{S}\cdot\text{cm}^{-1}$ at the rest (Table 13). In addition, average ^{222}Rn at P2 was $7693 \text{ Bq}\cdot\text{m}^{-3}$ compared to $2319 \text{ Bq}\cdot\text{m}^{-3}$ at the rest. Average ^{223}Ra at P2 was $940 \text{ dpm}\cdot\text{m}^{-3}$ compared to $399 \text{ dpm}\cdot\text{m}^{-3}$ at the rest and average ^{224}Ra was $13853 \text{ dpm}\cdot\text{m}^{-3}$ at P2 compared to $6262 \text{ dpm}\cdot\text{m}^{-3}$ at the rest (Table 2, 4, 5). Although these documented differences support a distinctive source of water at P2, that source is not readily identifiable with any of the endmembers in this study. However, some relationship between P2 and the deep well could be argued upon. Average measured conductivity in P2 was $47525 (\mu\text{S}\cdot\text{cm}^{-1})$

¹) compared to 48460 $\mu\text{S}\cdot\text{cm}^{-1}$ in the deep well, average ^{222}Rn in P2 was 7692 $\text{Bq}\cdot\text{m}^{-3}$ compared to 4726 $\text{Bq}\cdot\text{m}^{-3}$ in the deep well, average ^{223}Ra in P2 was 940 $\text{dpm}\cdot\text{m}^{-3}$ compared to 1124 $\text{dpm}\cdot\text{m}^{-3}$ in the deep well, and average ^{224}Ra in P2 was 13853 $\text{dpm}\cdot\text{m}^{-3}$ compared to 8943 $\text{dpm}\cdot\text{m}^{-3}$ in the deep well (Table 2, 4, 5). While the sample size is small and these parameters are not identical, it must be noted that the location of these samples are spaced approximately 100 m apart laterally and are, thus, susceptible to significant mixing from unrealized sources. This is likely as the first samples collected at the deep well were extremely uncharacteristic of the site, with a measured conductivity of 479 $\mu\text{S}\cdot\text{cm}^{-1}$.

A possible explanation for the enhanced effectiveness of the models at P2 compared to the other piezometers is the method's relative inability to resolve the near surface "recirculated zone". In studying the hydrologic properties of a coastal wetland via ERT, Musgrave and Binley (2011) notes that changes in temperature in the subsurface may be dominated by conduction rather than advection as documented by (McKenzie et al., 2007). Under the assumption that poorly constrained temperature values at P1, P3, P4, and P6 are related to changes in ambient temperature at the surface, those changes are likely explained by conductive forces driving the recirculation of seawater in the near surface.

As previously mentioned, there is no significant difference in the calculations produced by the Waxman-Smits equation and Archie's Law. Both methods produce an average flux of $\sim 26 \text{ cm}\cdot\text{d}^{-1}$ (Table 11, 12). Additionally, using ^{222}Rn , the shallow well, deep well, and average watershed endmembers produce discharge rates on the same order of magnitude, but more than double the former value (Table 2, 3). Also, the ^{223}Ra deep well endmember, the ^{224}Ra deep well and groundwater well, as well as the ^{226}Ra

endmembers are the only radium isotope calculations which provide agreeable results at 49, 80, 39, and 21 $\text{cm}\cdot\text{d}^{-1}$, respectively (Table 7, 8, 9). Under the premise that P2 represents a source or conduit associated with the deep well unit within the study area, it is significant that the deep well endmember was prevalent across each radiogenic isotope as the ERT model was objectively the most successful in resolving data at P2 (Figure 17, 18).

While this is suggestive of a correlation between the radiogenic isotopes and ERT models in quantifying SGD, there is no explicit relationship between the two supported by statistical analyses. When considering ^{224}Ra , the shortest-lived Ra isotope with a half-life of 3.66 days, there exists an anticipated positive correlation between measured fluid SPC and associated ^{224}Ra activities ($R^2=0.7294$, $p\text{-value}=0.0001$, $n=21$) (Figure 9 (b)). In comparison, there is very little relationship between fluid conductivities produced by the ERT model and ^{224}Ra activities ($R^2=0.069$, $p\text{-value}=0.76601$, $n=21$) (Figure 9 (a)).

Because ^{224}Ra activities have a significant correlation with constrained fluid conductivity, any misfit between ^{224}Ra activities and ERT model conductivities could be associated with latent variable influence related to ERT bulk conductivity (Cai et al., 2015). If the predominant latent variable is temperature in this case, then it would be intuitive to evaluate the relation between ^{224}Ra and fluid conductivity at P2 in comparison to the other piezometers in reference to Figure 19. When cumulatively assessing P1, P3, P4, and P6, the correlation returns $R^2=0.0009$, $p\text{-value}=0.9972$, $n=18$. In turn, P2 returns $R^2=0.7916$, $p\text{-value}=0.2858$, $n=3$. Although neither correlation proved significant, the lack of significance in P2 is likely the result of a small sample size.

One consideration not made in estimating SGD using ERT was the effect of error propagating through the calculations, beginning with the removal of data during processing based on percent misfit and ending with the final SGD rate. While the model may have an overall error of less than 3% in most cases, there are still relative outliers which fall just under the 10% threshold. Furthermore, if data is removed in one timestep, but not another, then there may be a section of the difference image which is not a legitimate representation of changes in the subsurface. It is an artifact produced through processing. Lastly, if data is removed at all, then care should be taken during interpretation post processing as the interpolation will likely have overlooked the section with no data and interpolated through it.

5. Summary

There are specific results to reestablish here in considering whether or not time-lapse ERT has a legitimate role in quantifying SGD in fine sediment and highly saline, shallow embayments. While Darcian estimates fell short, all four of the radiogenic isotopes and the time-lapse ERT produced comparable SGD rates on the same order of magnitude by employing or inferring very similar endmembers/sources, namely the deep well unit. In addition, after performing well constrained data analyses, a best practice workflow and future suggestions have been objectively established for ERT model processing and interpretation with respect to this type of environment.

While these results are encouraging at the surface level, there are further considerations to be made. First, the objective of this study was to evaluate the feasibility of the time-lapse ERT method. Although final SGD rates were acceptable, obtaining these

data required detailed constraints of the subsurface which are not readily available in most of the remote locations along the Texas Gulf Coast where sampling has occurred in the past and may occur in the future. Hard constraints like these provide confidence in the results which may be otherwise unattainable. Such is the ambiguous, nonunique nature of subsurface geophysics. For this work to be feasible, similar measures should be taken to ensure quality control.

Second is the propagation of error in calculating SGD rates using ERT. There is inherent error associated with the original bulk conductivity measurements and subsequent error associated with the derivation of fluid conductivity values. In this study, error was accounted for during interpretation by using the RMS error produced during individual model inversions to define a minimum threshold for changes in conductivity to be considered significant enough to be assumed potential SGD.

Lastly, the effectiveness of the ERT method in resolving potential errors and artifacts with respect to the recirculated zone in the upper 1m of the model is still in question. As previously mentioned, temperature appears to be the predominant variable of influence in this region. Temperature was not well accounted for in planning the survey and could have been constrained much more effectively by monitoring it at a higher spatial and temporal resolution and producing models which have been corrected for subsurface temperature prior to inversion. The perceived lack of constraints on temperature was further exacerbated by the drastic changes in which occurred between day and night during data collection (low of 2.7° C, high of 23.3° C) and relatively low surface water levels along the profile (0.2 -1 m).

Per the results of correlating modeled conductivity with measured conductivity at P2, fluid conductivity calculations are much more accurate when the influence of temperature is well constrained. It is uncertain why temperature was so relatively well constrained at the location. As already stated, it could be that the piezometer was installed in such a way that minimized any potential mixing with the surface water which was subject to the extreme ambient temperature inversions. In addition, the importance of resolving the variable influence of temperature is further supported by the results of correlating modeled conductivity with ^{224}Ra . Although the P2 correlation was not significant, it was in fact much more significant relative to the cumulative correlation performed with P1, P3, P4, and P6. Intuition would then suggest that a larger sample size would produce much more effective results. A potential correlation with the shorter-lived ^{224}Ra isotope is worth investigating given that the temporal SGD rates ultimately produced by both methods can be functions of changes in salinity, among other things. Hence the importance of resolving the temperature component in ERT.

This investigation has laid the foundation for potential work with respect to near-surface geophysics in its application to SGD along the Texas Gulf Coast. Recommendations have been made in regard to survey design, data processing and interpretation, and items of interest to consider in future investigations. While time-lapse ERT seems to have an undefined role in studying SGD, further work must be done to fully evaluate and refine the methodology.

Literature Cited

- Abraham, D.M., Charette, M.A., Allen, M.C., Rago, A., Kroger, K.D. (2003) Radiochemical Estimates of Submarine Groundwater Discharge to Waquoit Bay, Massachusetts. *Biological Bulletin* 205, 2.
- AGI (2008) *EarthImager2DManual*.
- ASFT&M (1999) *Standard Guide for Selection of Aquifer Test Method in Determining Hydraulic Properties by Well Techniques* 1.
- Avnimelech, Y., Ritvo, G., Meijer, L.E., Kochba, M. (2001) Water content, organic carbon and dry bulk density in flooded sediments. *Aquacultural Engineering* 25, 25-33.
- Bache, B.W. (1975) The Measurement of Cation Exchange Capacity of Soils *J. Sci. Fd Agric.* 27, 7.
- Baudron, P., Cockenpot, S., Lopez-Castejon, F., Radakovitch, O., Gilabert, J., Mayer, A., Garcia-Arostegui, J.L., Martinez-Vicente, D., Leduc, C., Claude, C. (2015) Combining radon, short-lived radium isotopes and hydrodynamic modeling to assess submarine groundwater discharge from an anthropized semiarid watershed to a Mediterranean lagoon (Mar Menor, SE Spain). *Journal of Hydrology* 525, 55-71.
- BENTALL, R. (1936) *Methods of Determining Permeability, Transmissibility and Drawdown - Groundwater Hydraulics*. Geological Survey Water-Supply 1536.
- Bighash, P., Murgulet, D. (2015) Application of factor analysis and electrical resistivity to understand groundwater contributions to coastal embayments in semi-arid and hypersaline coastal settings. *Sci Total Environ* 532, 688-701.
- Breier, J.A., Breier, C.F., Edmonds, H.N. (2005) Detecting submarine groundwater discharge with synoptic surveys of sediment resistivity, radium, and salinity. *Geophysical Research Letters* 32.
- Burnett, W.C., Dulaiova, H. (2003) Estimating the dynamics of groundwater input into the coastal zone via continuous radon-222 measurements. *Journal of Environmental Radioactivity* 69, 21-35.
- Cai, P., Shi, X., Hong, Q., Li, Q., Liu, L., Guo, X., Dai, M. (2015) Using $^{224}\text{Ra}/^{228}\text{Th}$ disequilibrium to quantify benthic fluxes of dissolved inorganic carbon and nutrients into the Pearl River Estuary. *Geochimica et Cosmochimica Acta* 170, 188-203.
- Cardenas, M.B., Zamora, P.B., Siringan, F.P., Lapus, M.R., Rodolfo, R.S., Jacinto, G.S., San Diego-McGlone, M.L., Villanoy, C.L., Cabrera, O., Senal, M.I. (2010) Linking regional sources and pathways for submarine groundwater discharge at a reef by electrical resistivity tomography, ^{222}Rn , and salinity measurements. *Geophysical Research Letters* 37, n/a-n/a.
- Carretero, S., Rapaglia, J., Perdomo, S., Albino Martínez, C., Rodrigues Capítulo, L., Gómez, L., Kruse, E. (2019) A multi-parameter study of groundwater–seawater

- interactions along Partido de La Costa, Buenos Aires Province, Argentina. *Environmental Earth Sciences* 78.
- Carroll, D. (1959) Ion Exchange in Clays and Other Minerals. *Bulletin of the Geological Society of America* 70, 31.
- Charette, M.A.M.C.A. (2006) Precision Ground Water Sampling in Coastal Aquifers Using a Direct-Push, Shielded-Screen Well-Point System. *Groundwater Monitoring & Remediation* 26, 7.
- Collette, L.a. (2006) A Method of Shaly Sand Correction for Estimating Gas Hydrate Saturations Using Downhole Electrical Resistivity Log Data. USGS.
- Cross, V.A. (2010) Continuous Resistivity Profiling and Seismic-Reflection Data Collected in April 2010 From Indian River Bay, Delaware.
- Dimova, N.T., Swarzenski, P.W., Dulaiova, H., Glenn, C.R. (2012) Utilizing multichannel electrical resistivity methods to examine the dynamics of the fresh water-seawater interface in two Hawaiian groundwater systems. *Journal of Geophysical Research: Oceans* 117, n/a-n/a.
- Eby, G.N. (2004) Principles of Environmental Geochemistry.
- Flores, R., Shindeler, G. (1986) Geochemistry and Mineralogy of Late Quaternary. USGS.
- Gregorich, M.R.C.E.G. (2006) Soil Sampling and Methods of Analysis. Chapter 18 - Ion Exchange and Exchangeable Cations.
- Harrison, A. (2006) Evaluating the reliability of continuous resistivity profiling to detect submarine groundwater discharge in a shallow marine environment: Sarasota Bay, Florida.
- Henderson, R.D., Day-Lewis, F.D., Abarca, E., Harvey, C.F., Karam, H.N., Liu, L., Lane, J.W. (2009) Marine electrical resistivity imaging of submarine groundwater discharge: sensitivity analysis and application in Waquoit Bay, Massachusetts, USA. *Hydrogeology Journal* 18, 173-185.
- Hunt, C.D. (1981) REGULATION OF SEDIMENTARY CATION EXCHANGE CAPACITY BY ORGANIC MATTER *Chemical Geology* 1, 18.
- Kim, G., et al. (2001) Measurement of ²²⁴Ra and ²²⁶Ra Activities in Natural Water Using a Radon-in-Air Monitor. *Environ. Sci. Technol.* 35, 4.
- Knee, K.L., Crook, E.D., Hench, J.L., Leichter, J.J., Paytan, A. (2016) Assessment of Submarine Groundwater Discharge (SGD) as a Source of Dissolved Radium and Nutrients to Moorea (French Polynesia) Coastal Waters. *Estuaries and Coasts* 39, 1651-1668.
- Leslie W. Lenfest, J. (2012) USER'S MANUAL FOR THE NATIONAL WATER INFORMATION SYSTEM OF THE U.S. GEOLOGICAL SURVEY. Groundwater Site Inventory-System 4.3.
- Lewis F.D., e.a. (2006) Continuous resistivity profiling to delineate submarine groundwater discharge—examples and limitations. *Society of Exploration Geophysics*.

- Loggers, o.H.D. Using the Conductivity Assistant: Calculating Specific Conductance with Sea Water.
- Loke, M.H., Chambers, J.E., Rucker, D.F., Kuras, O., Wilkinson, P.B. (2013) Recent developments in the direct-current geoelectrical imaging method. *Journal of Applied Geophysics* 95, 135-156.
- Loke, M.H., Lane Jr, J.W. (2004) Inversion of data from electrical resistivity imaging surveys in water-covered areas. *Exploration Geophysics* 35, 266.
- Manheim, F.T. (2004) Studying Ground Water Under Delmarva Coastal Bays Using Electrical Resistivity. *GroundWater*.
- McCoy, C.A., Corbett, D.R. (2009) Review of submarine groundwater discharge (SGD) in coastal zones of the Southeast and Gulf Coast regions of the United States with management implications. *J Environ Manage* 90, 644-651.
- McKenzie, J.M., Siegel, D.I., Rosenberry, D.O., Glaser, P.H., Voss, C.I. (2007) Heat transport in the Red Lake Bog, Glacial Lake Agassiz Peatlands. *Hydrological Processes* 21, 369-378.
- Michael, H.A., Lubetsky, J.S., Harvey, C.F. (2003) Characterizing submarine groundwater discharge: A seepage meter study in Waquoit Bay, Massachusetts. *Geophysical Research Letters* 30.
- Millero, F. (2010) History of the Equation of State of Seawater. *Oceanography* 23, 18-33.
- Moore, W.S. (2010) The effect of submarine groundwater discharge on the ocean. *Ann Rev Mar Sci* 2, 59-88.
- Moore, W.S., Arnold, R. (1996) Measurement of ^{223}Ra and ^{224}Ra in coastal waters using a delayed coincidence counter. *Journal of Geophysical Research: Oceans* 101, 1321-1329.
- Moore, W.S., Reid, D.F. (1973) Extraction of radium from natural waters using manganese-impregnated acrylic fibers. *Journal of Geophysical Research* 78, 8880-8886.
- Mulligan, A.E., Charette, M.A. (2006) Intercomparison of submarine groundwater discharge estimates from a sandy unconfined aquifer. *Journal of Hydrology* 327, 411-425.
- Murgulet, D., Murgulet, V., Spalt, N., Douglas, A., Hay, R.G. (2016) Impact of hydrological alterations on river-groundwater exchange and water quality in a semi-arid area: Nueces River, Texas. *Sci Total Environ* 572, 595-607.
- Musgrave, H., Binley, A. (2011) Revealing the temporal dynamics of subsurface temperature in a wetland using time-lapse geophysics. *Journal of Hydrology* 396, 258-266.
- Oberdorfer, J. (2003) Hydrogeologic modeling of submarine groundwater discharge: comparison to other quantitative methods. *Biogeochemistry* 66, 11.
- Ogilvy, R.D., Kuras, O., Meldrum, P.I., Wilkinson, P.B., Gisbert, J., Jorreto, S., Frances, I., Pulido Bosch, A. (2009) Automated time-lapse electrical resistivity tomography (ALERT) for monitoring coastal aquifers. *Near Surface Geophysics* 7, 367-375.

- Onovughe, S. (2016) Saturation Modelling: Using The WaxmanSmits Model/Equation In Saturation Determination In Dispersed Shaly Sands. *Journal of Multidisciplinary Engineering Science and Technology (JMEST)* 3.
- Orlando, L. (2013) Some considerations on electrical resistivity imaging for characterization of waterbed sediments. *Journal of Applied Geophysics* 95, 77-89.
- Peterson, R.N., Burnett, W.C., Taniguchi, M., Chen, J., Santos, I.R., Ishitobi, T. (2008) Radon and radium isotope assessment of submarine groundwater discharge in the Yellow River delta, China. *Journal of Geophysical Research* 113.
- Pidlisecky, A., Knight, R. (2008) FW2_5D: A MATLAB 2.5-D electrical resistivity modeling code. *Computers & Geosciences* 34, 1645-1654.
- R.A. Morton, C.D.W. (1979) Distribution and Significance of Coarse Biogenic and Clastic Deposits on the Texas Inner Shelf. Texas General Land Office.
- Santos, I.R., Burnett, W.C., Chanton, J., Dimova, N., Peterson, R.N. (2009) Land or ocean?: Assessing the driving forces of submarine groundwater discharge at a coastal site in the Gulf of Mexico. *Journal of Geophysical Research* 114.
- Smith, C.G., L.L., Robbins (2012) Surface-Water Radon-222 Distribution along the West-Central Florida Shelf.
- Swarzenski, e.a. (2007) Geochemical and Geophysical Examination of Submarine Groundwater Discharge and Associated Nutrient Loading Estimates into Lynch Cove, Hood Canal, WA. *Environmental Science & Technology* 41, 7.
- Swarzenski, P.W., Burnett, W.C., Greenwood, W.J., Herut, B., Peterson, R., Dimova, N., Shalem, Y., Yechieli, Y., Weinstein, Y. (2006) Combined time-series resistivity and geochemical tracer techniques to examine submarine groundwater discharge at Dor Beach, Israel. *Geophysical Research Letters* 33.
- USGS (2010) Conducting an Instantaneous Change in Head (Slug) Test with a Mechanical Slug and Submersible Pressure Transducer. USGS.
- Vasantrao, B.M., Bhaskarrao, P.J., Mukund, B.A., Baburao, G.R., Narayan, P.S. (2017) Comparative study of Wenner and Schlumberger electrical resistivity method for groundwater investigation: a case study from Dhule district (M.S.), India. *Applied Water Science* 7, 4321-4340.
- Viso, R., McCoy, C., Gayes, P., Quafisi, D. (2010) Geological controls on submarine groundwater discharge in Long Bay, South Carolina (USA). *Continental Shelf Research* 30, 335-341.
- Welschmeyer, N.A. (1994) Fluorometric Analysis of Chlorophyll a in the Presence of Chlorophyll b and Pheopigments. *Limnology and Oceanography* 39.
- Williams, D.D. (2005) Monitoring, Analysis and Interpretation of the Post-Construction Evolution of a Restored Beach at TAMU-CC. Texas General Land Office Coastal Management Program.
- Zarroca, M., Linares, R., Rodellas, V., Garcia-Orellana, J., Roqué, C., Bach, J., Masqué, P. (2014) Delineating coastal groundwater discharge processes in a wetland area by means of electrical resistivity imaging, ^{224}Ra and ^{222}Rn . *Hydrological Processes* 28, 2382-2395.